Department of Physics and Astronomy

University of Heidelberg

Bachelor thesis

in Physics

submitted by

Jan Patrick Hammerich

born in Heidelberg

2015

Studies of HV-MAPS

Analog Performance

This Bachelor thesis has been carried out by

Jan Patrick Hammerich

at the

Physikalisches Institut Heidelberg

under the supervision of

Prof. Dr. André Schöning

Zusammenfassung Das Mu3e Experiment wird nach dem Leptonenflavorzahl verletzenden Zerfall $\mu^+ \to e^+e^-e^+$ suchen. Dieser Zerfall ist im Standard Model auf ein Verzweigungsverhältnis von $< 10^{-54}$ unterdrückt, so dass eine Beobachtung dieses Zerfalls auf Physik jenseits des Standardmodells hinweisen würde. Die Zielsensitivität des Experiments ist 1 in 10^{15} Myonenzerfällen, wofür einen Myonenstrahl mit einer Intensität von 10^8 Myonen pro Sekunde benötigt wird, die an einem Target gestoppt werden und zerfallen.
Weil die Myonen in Ruhe zerfallen ist die maximale Energie eines Teilchens im Endzustand 53MeV. Dies führt dazu, dass Mehrfachstreuung die dominiernde Fehlerquelle bei der Spurenrekonstruktion darstellt, weswegen die Materialmenge des Detektors so gering wie möglich gehalten muss. Um die Zielsensitivität bei hoher Zerfallsrate zu erzielen, werden eine gute Orts- und Zeitauflösung benötigt. Eine Technologie die alle Anforderungen erfüllt ist das Hochspannungs Monolitische Aktive Pixel Sensoren (HV-MAPS) Konzept. HV-MAPS können in kommerziellen CMOS Prozessen produziert und auf 50µm gedünnt werden. HV-MAPS kombinieren integrierte digitale und analoge Elektronik mit aktivem Sensor auf einem Chip um Materialmenge und Kosten zu reduzieren.
Für diese Arbeit wurden zwei aktuelle HV-MAPS Prototypen für das Mu3e Experiment, der MuPix4 und der MuPix6, auf ihre Unterschiede untersucht. Der MuPix7, der neuste Prototyp, wurde außerdem getestet um die Übereinstimmung mit dem MuPix6 Analogdesign zu überprüfen.
Zusätzlich werden Resultate für das individuelle justieren der Schwellenwerte für jedes Pixel, das so genannte Tuning, gezeigt und Tuningmethoden diskutiert.

Abstract The Mu3e experiment will search for the lepton flavor violating decay $\mu^+ \to e^+e^-e^+$. This decay is suppressed to a branching ratio of $< 10^{-54}$ in the Standard Model so any observation of this decay would indicate physics beyond the Standard Model. The target sensitivity of the experiment is 1 in 10^{15} muon decays, which requires a muon beam with an intensity of 10^8 muons per second which are stopped at a target and decay.
Because the muons decay at rest, the maximum energy of a final state particle is 53MeV. This causes multiple Coulomb scattering to be the dominant error source for the tracking so the material budget has to be as small as possible. To achieve the target sensitivity at a high decay rate, good time and spatial resolution are required. A technology that fulfills all specifications is the High Voltage Monolithic Active Pixel Sensor (HV-MAPS) concept. This design allows for sensors to be commercially produced and thinned to 50µm. HV-MAPS integrate the digital and analog electronics in the same chip as the sensitive region to reduce material budget and production costs. For this thesis, two current HV-MAPS prototypes for the Mu3e experiment, the MuPix4 and MuPix6, have been studied in respect to their differences. The MuPix7, the newest prototype, was also tested to confirm parity with the Mupix6 analog design.
Additionally, results from adjusting the threshold of each pixel individually, the so called tuning, are presented and tuning methods are discussed.

Contents

Part I

Introduction

1 Introduction

Most of the present knowledge about particles and their interactions is compiled in the Standard Model of Particle Physics (SM). It describes the known particles and their interactions with each other and has been very successful over the last decades. However, there are phenomena that the Standard Model can not explain or even describe. Energy regions which are not well described by perturbative calculations, gravity or the composition of the universe's matter are examples. To explain and describe these processes many new theories have been developed to fill the gap of knowledge.
There are multiple ways to test the predictions of these new theories. The direct approach is to look for new particles, which are predicted at high energy scales, which is done at the LHC. The indirect search for new physics includes measuring branching ratios of decays and reactions to very high precision as unknown particles can leave footprints in these processes when they enter via quantum loops. This means a significant deviation from the SM prediction or the observation of a forbidden process indicate new physics. To achieve the required precision, large numbers of decays have to be measured which requires high rates and high precision detectors.
One of these experiments at the intensity frontier is the Mu3e experiment which is proposed to measure the branching fraction of the charged lepton flavor violating decay $\mu^+ \to e^+e^-e^+$ to a sensitivity of 1 in 10^{15} at 90% confidence level [1].
To achieve this limit in a few years of operation, $\mathcal{O}(10^8)$ muon decays per second have to be measured. The muons are provided by the High Intensity Proton Accelerator (HIPA) at the Paul Scherrer Institute (PSI) in Switzerland. The muons are stopped at a target and decay at rest. Therefore, the momentum of the decay products is limited to half the muon mass with 53MeV which gives a strong constraint on the material budget to reduce multiple Coulomb scattering.
For that reason, the detector consists of cylindrical layers of thin silicon sensors mounted on a Kapton® frame along the beam axis. Scintillating fibers provide additional time information. The detector is placed in a magnetic field to measure the particle momenta. Upstream and downstream of the target more modules out of silicon pixels and scintillating tiles are placed to measure recurling particles, giving precise momentum and time measurements.
A technology to provide such thin silicon sensors is the High Voltage Monolithic Active Pixel Sensor (HV-MAPS) concept. This technology combines the idea of Monolithic Active Pixel Sensors (MAPS), where sensor and readout are combined into one chip, with a high voltage (HV) depleted diode as detection volume which allows for fast signal collection. Because the depletion zone is only about 10µm thick, chips can be thinned down industrially. Chips thinned to 50µm have been successfully operated so far. The production process is a standard commercial HV-CMOS process which allows production at low costs.

In this thesis characterization measurements of the latest HV-MAPS prototypes for the Mu3e experiment, the MuPix chips, are presented. These chips have been tested in the lab and also in test beam campaigns.
The MuPix4 is the first working prototype with integrated readout, which was also tested in a thinned version. The MuPix6 is the successor of the MuPix4. It has an improved digital readout and an additional amplification stage to achieve a better signal to noise separation. The MuPix7 is the newest prototype and incorporates new digital features such as an internal state machine and a fast serial data output. For the MuPix7 analog measurements to check for consistency with the MuPix6 have been performed.
The MuPix4 and MuPix6 have been measured in respect to their response to various signals, such as X-rays, testpulses and γ radiation. These are important factors to determine future designs and are necessary for finding an operation point for the experiment. For the MuPix6 and MuPix7 a minimal detection energy of $\approx$ 2keV was extrapolated which is half of the expected mean signal for the experiment with $\approx$ 4keV. For the MuPix6 methods to improve the performance of the chip by adjusting the threshold of the pixels individually, the so called "tuning", are described and the improvements quantified. The noise rate of over 1.5kHz per pixel for over 50% of the pixels was reduced to $\leq$ 1Hz per pixel for almost all pixels. The full width half maximum of the noise threshold distribution of $\approx$ 35mV was reduced to $\approx$ 10mV.

2 Theory

2.1 The Standard Model of Particle Physics

The Standard Model of Particle Physics (SM) unifies the known particles and their interactions in a theory framework. It reduces the "particle zoo" to twelve elemental fermions, their anti-particles and gauge bosons, which mediate the fundamental forces: the electromagnetic force as well as the strong and weak force. So far gravitation could not be measured on quantum level and is therefore not included. It's effects are also many orders of magnitude weaker than any of the other forces so that gravity can be neglected.

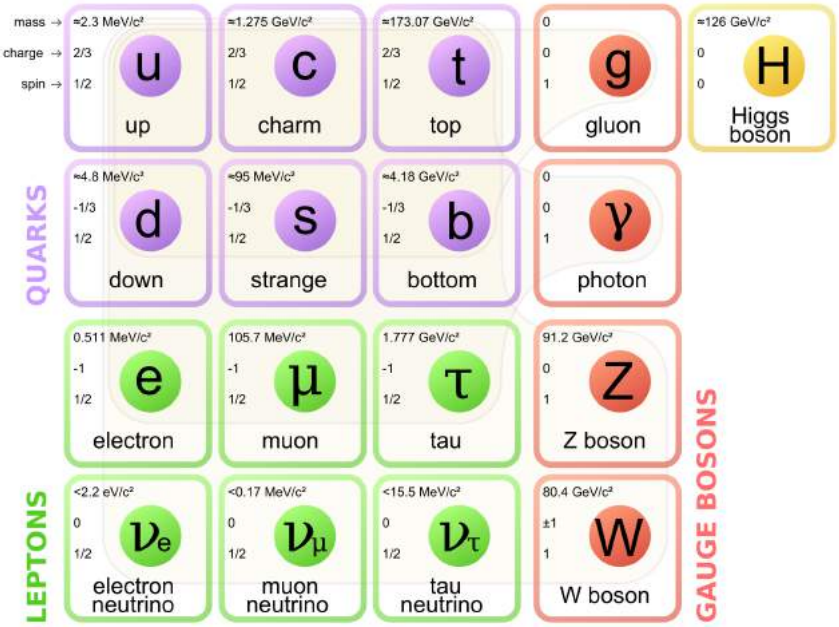

Figure 2.1: The elementary particles of the Standard Model of Particle Physics [2]

These particles are categorized by their mass and quantum numbers such as spin, electric and weak hyper charge, color and flavor. This divides the fermions into quark-type particles who carry color charge and leptons who are "colorless". Both families are subdivided into three generations by their mass and flavor.

The quarks consist of three generations of up-type and down-type quarks with increasing masses. The up-type quarks are electrically charged with +2/3 of the electron charge and are named up (u), charm (c) and top (t). The down-type quarks carry only -1/3 elementary charge and are called down (d), strange (s) and bottom (b). These particles couple to all fundamental forces.
The leptons consist of the three leptons with -1 electric charge, the electron (e), the muon (μ) and the tau (τ), and their respective chargeless neutrinos (ν). The charged leptons interact weak and electric while the neutrinos interact purely weak. In the SM the neutrinos are treated as massless particles.
This leaves the gauge bosons which mediate the forces. The massless photon (γ) mediates the electro-magnetic force (EM) by coupling to electric charge. The weak mediators are the charged W-bosons at 80.4GeV mass with ± 1 electron charge and the neutral Z-boson at 91.2GeV mass. The strong force is more complicated as its carrier, the massless gluon (g) carries color charge itself so it allows coupling to other gluons. The strong interactions are described by the theory of Quantum Chromo Dynamics (QCD). Because of its selfcoupling, the range of strong interaction is limited, leading to groupings of particles with no net color, so called hadrons.
In the SM the electro-magnetic and weak force can be unified to the so called electroweak force with 4 massless gauge bosons. Because the weak mediators do have mass, a mechanism is necessary to cause this symmetry breaking. This mechanism is called Higgs mechanism, which predicts the Higgs boson which was recently discovered at the LHC ([3] & [4]).
The eigenstates of different forces are not the same for some cases, e.g. the weak eigenstates are superpositions of strong eigenstates which causes the weak force to violate quark flavor. This mixing relation is described by the Cabibbo-Kobayashi-Maskawa-Matrix (CKM-Matrix).
For a long time lepton flavor was thought of as a conserved quantity until flavor oscillation in neutrinos ([5, 6, 7]) had been discovered. This indicates that neutrinos are in fact not massless. The violation of lepton flavor (LFV) for charge leptons hasn't been observed so far.
Although the SM has a history of successes, unsolved problems like neutrino mixing, gravity, dark matter particles and matter/anti-matter asymmetry have led to a wide field of theories beyond the SM which predict new particles at various masses above the well measured energy ranges.

2.2 The Muon Decay

2.2.1 In the Standard Model

The SM muon has only one leading order decay channel, the Michel decay $\mu^- \to e^- \nu_\mu \bar{\nu}_e$. In next to leading order, the radiative decay $\mu^- \to \gamma e^- \nu_\mu \bar{\nu}_e$ and the internal conversion decay $\mu^+ \to e^+ e^- e^+ \bar{\nu_\mu} \nu_e$ come into play [8].
As lepton flavor was considered a conserved quantity in the SM , decays like $\mu^+ \to e^+ e^- e^+$ were forbidden. With the addition of neutrino mixing charged LFV can be allowed in loop diagrams like in Fig. 2.2 which shows the most dominant decay channel. The branching ratio (BR) of this decay however would be suppressed by the mass ratio $\frac{(\Delta m^2_\nu)^2}{m^4_W}$ which yields a $BR < 10^{-54}$ which is not observable.
The related decay $\mu \to e\gamma$ is less suppressed due to the missing vertex factor of α_{em}.
Any statistically significant signal of these decays would indicate a unknown physics process that is beyond the Standard Model description.

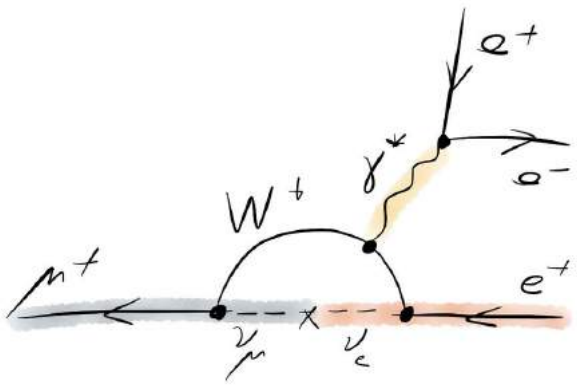

Figure 2.2: Loop diagram for a neutrino mixing induced $\mu \to eee$ decay

2.2.2 Beyond the Standard Model

As seen in section 2.2.1, charged lepton flavor is conserved in leading order in the SM. Theories beyond the Standard Model include charged LFV (cLFV) which contribute to the BR and could increase it to measurable levels. These predictions are constrained by the current experimental limits at 90% confidence level with $BR < 10^{-12}$ for $\mu^+ \to e^+ e^- e^+$ [9] and $\mu \to e\gamma$ with $BR < 5.7 \times 10^{-13}$ [10].
These enhancements come from proposed heavy mediator particles at tree level like in Fig. 2.3(b) or via Super Symmetric (SUSY) particles via loop diagrams as seen in Fig. 2.3(a).

However, these processes are suppressed by the large masses of the involved particles so their contributions are still very small.

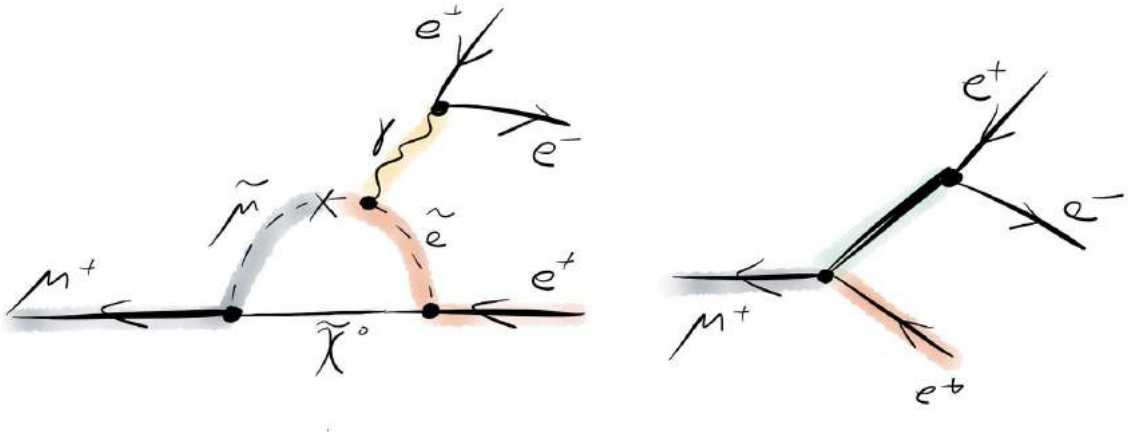

(a) $\mu \to eee$ at loop level mediated by supersymmetric partners

(b) $\mu \to eee$ at tree level with a heavy mediator

Figure 2.3: $\mu \to eee$ beyond the SM

3 The Mu3e Experiment

The Mu3e experiment aims to measure the BR of the LFV decay $\mu^+ \to e^+e^-e^+$ with a precision of 1 in 10^{15} or better. To achieve this sensitivity in a few years of running, 10^8 muon decays per second have to be measured.
This chapter describes the status of LFV decay searches as well the concept and design of the Mu3e detector.

3.1 Status of LFV Decay Searches

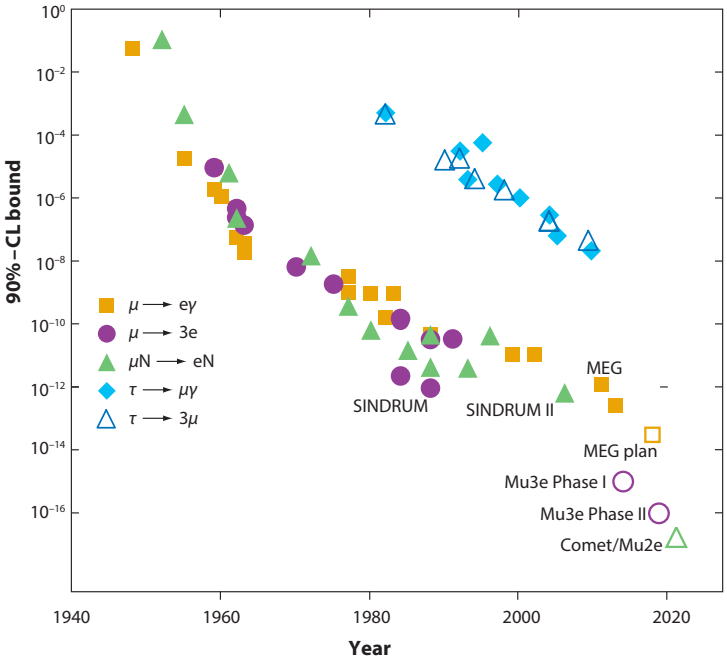

Figure 3.1: Measured and planned limits on LFV decays. Adapted from [11].

3.1.1 SINDRUM

The SINDRUM experiment searched from 1983-1986 for the decay $\mu^+ \to e^+e^-e^+$. As no signal was found, the upper limit for the BR was calculated to be $< 10^{-12}$ at 90% confidence level (CL) [9].
The experiment was conducted at the PSI, where 28MeV/c muons were stopped on a double cone target in a 0.33T magnetic field. The detection volume consisted 5 layers of Multi-Wire-Proportional Chambers (MWPC) triggered by a hodoscope. The internal conversion decay $\mu^+ \to e^+e^-e^+\bar{\nu_\mu}\nu_e$, which was the biggest background, was estimated to 5×10^{-14}. The experimental results of SINDRUM are limited by the number of observed muon decays.

3.1.2 MEG

The MEG experiment [12] is currently undergoing an upgrade but ran since 2008 at PSI and searched for LFV decay $\mu \to e\gamma$. It consists of a liquid Xe calorimeter to detect photons and a drift chamber to detect the positrons as anti-muons were observed.
The limit set by MEG on this decay is $< 5.7 \times 10^{-13}$ at 90% [12] with an expected limit of 1×10^{-13} after the upgrade. This corresponds to a sensitivity of 1 in 10^{15} for the $\mu \to eee$ decay as the $\mu \to eee$ decay is suppressed by α_{em} compared to the $\mu \to e\gamma$ decay.

3.1.3 Conversion Experiments

A third possible cLFV is the conversion $\mu \to e$ with nuclei. This would result in monoenergetic electrons at energies outside of the range of Michel decay electrons.
The limit set by SINDRUM II, which measured the process $\mu Au \to eAu$ to a BR $< 7 \times 10^{-13}$ [13], is the current best limit on conversion experiments with muons. New planned experiments at Fermilab with Mu2e or at J-PARC with DeeMe, PRISM and COMET seek to to improve this limit up to BR $< 10^{-14}$ to $< 10^{-16}$.

3.2 Signal Decay

Because the mediator of the $\mu^+ \to e^+e^-e^+$ decay is much heavier than the invariant mass of the muon, it is only considered virtual, which means that it has no free path length, so the three electrons share a common vertex. Considering momentum conservation, the sum of the momenta of the electrons has to be zero for a muon at rest.

$$|\vec{p}_{tot}| = |\sum_{i=1}^{3} \vec{p}_i| = 0 \tag{3.1}$$

To conserve the energy of the muon, the electron energies have to add up to m_μ.

$$E_{tot} = |\sum_{i=1}^{3} E_i| = m_\mu \cdot c^2 \tag{3.2}$$

As result, the energy range for the decay products is from 0 to half the muon mass at ≈ 53MeV.
These relations allow to separate signal from background.

3.3 Background

The background for the $\mu \to eee$ decay can be split into two categories. The accidental background stems from limited resolution, which allows decays with very close vertices in time and space to look like the signal decay if not all decay products are detected.
The irreducible background originates from physics processes like the internal conversion decay $\mu^+ \to e^+e^-e^+\bar{\nu_\mu}\nu_e$.

3.3.1 Internal Conversion Background

The internal conversion decay $\mu^+ \to e^+e^-e^+\bar{\nu_\mu}\nu_e$ (Fig. 3.2) makes up the physics background. However, due to the neutrinos, which the detector can't measure, the total momentum and energy are different from a muon at rest.
To discriminate against this background while reaching a sensitivity of 1 in 10^{15} at 90% CL, the energy resolution has to be better than 1MeV [1].

Figure 3.2: Internal conversion decay in the SM

3.3.2 Accidental Background

Accidental background arises from high occupancy in the detector. This causes independent decay products to look like they come from a common vertex and are coincident in time. Fig. 3.3 gives an example: Fig. 3.3(a) shows the topology of a signal decay and Fig. 3.3(b) shows the topology of three decays with close vertices. Because the muon beam rate and the resulting muon decay rate in the Mu3e detector is very high, this background gives a significant contribution. To suppress this background as good as possible good timing and spacial resolution are necessary in order to precisely probe coincidence in space and time of all decay products of a signal decay candidate.

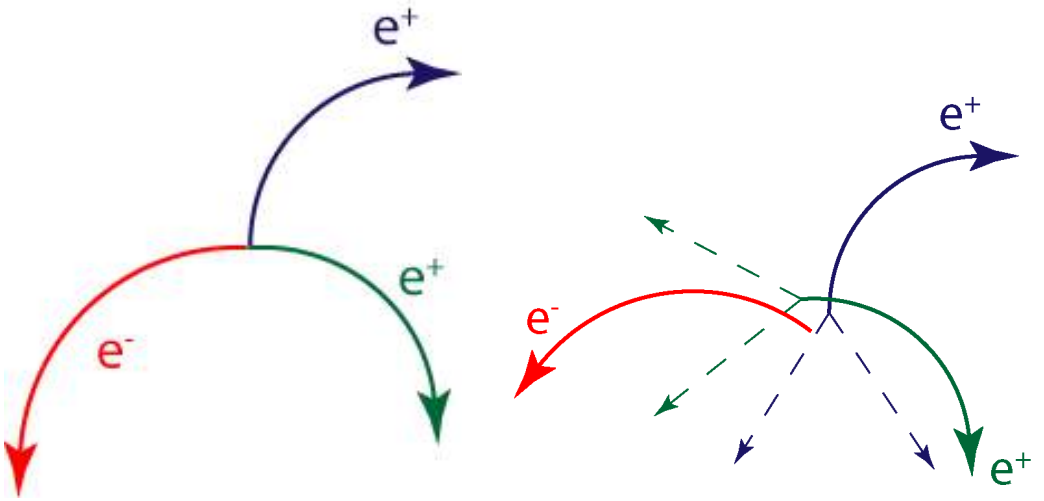

(a) Signal topology

(b) Accidental topology looking like a signal event

Figure 3.3: $\mu \to eee$ event topologies

3.4 The Mu3e Detector

The Mu3e detector is a barrel shaped detector surrounding a double-cone target on which muons are stopped an decay at rest. The target is surrounded by cylinders made out of thin, silicon pixel layers on a Kapton® support structure. Scintillating fibers give an additional timing information to suppress combinatorics. The 1T magnetic field not only allows to discriminate between positrons and electrons but bends the track of these low momentum particles such that they reenter the detector at the recurl-stations up- and downstream, which are made of silicon pixel layers and scintillating tiles. The recurl-stations increase the acceptance for recurling particles and add another set of spacial and timing information to improve the momentum and time resolution even more. The inner volume is gaseous helium which acts as coolant and has a low contribution to multiple Coulomb scattering. In total, the effective radiation length per layer will be $\approx 1‰$.
The detector will be placed at the $\pi E5$ beam line at the HIPA at PSI (Fig. 3.5). For this beam line, the 590MeV primary protons are colliding with a carbon target producing surface muons which are then extracted at 28MeV/c.

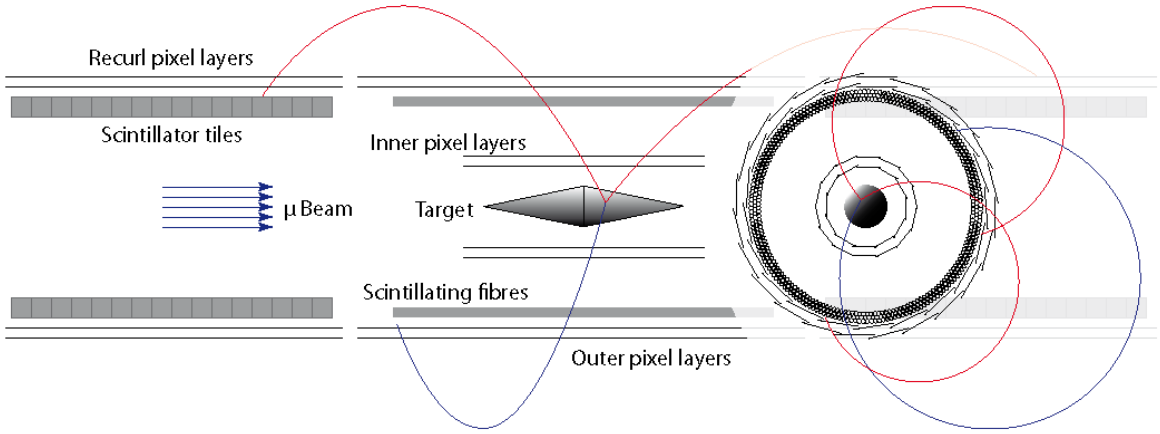

Figure 3.4: Design of the Mu3e detector with a $\mu \to eee$ decay. The view on the right side is along the beam axis.

Figure 3.5: PSI accelerator area with the $\pi E5$ beam line

4 Detection of Charged Particles and their Interaction with Matter

To detect particles one needs to observe their interaction with matter to deduce the particle's properties. This in turn influences the particle's properties and induces errors such as scattering. Scattering is an important effect for the Mu3e detector, the knowledge of how particles behave as they pass through matter is vital.

4.1 Interaction with Matter

The interaction of charged particles with matter depends strongly on the properties of the material as well as the properties of the particle itself. Charge z of the particle determines the strength of electro-magnetic interactions while mass factors in for kinematic effects like bremsstrahlung. Strong interactions of hadrons also factor in but they can be neglected for the Mu3e experiment as only electrons will be measured.

4.1.1 Heavy Particles

In particle physics "heavy" usually describes particles with $m_0 \geq 100\text{MeV}$. For those particles the main loss of energy by traversing matter is ionization up to very high energies in the GeV regime. The mean energy loss per length of material $\left\langle \frac{dE}{dx} \right\rangle$ is given by the Bethe-Bloch-formular given in Eq. 4.1 [14].

$$-\left\langle \frac{dE}{dx} \right\rangle = \frac{4\pi n z^2}{m_e c^2 \beta^2} \cdot \left(\frac{e^2}{4\pi\epsilon_0} \right)^2 \cdot \left[\log\left(\frac{2 m_e c^2 \beta^2}{I \cdot (1-\beta^2)} \right) - \beta^2 \right] \tag{4.1}$$

With:

- the relative velocity of the particle $\beta = \frac{v}{c}$
- the charge of the particle z
- the electron density of the material n
- the mean excitation energy I of the material
- and the constants electron mass rest m_e, the vacuum speed of light c and the vacuum permittivity ϵ_0

The function is drawn in Fig. 4.1.1 for different materials. It shows a minimum for $\frac{p}{m_0 c} \approx 3$ which is independent of the particle, meaning that each particle has a momentum range where it loses the least energy. Particles at their respective minimal ionizing momentum are called Minimum Ionizing Particles (MIP). The rise for higher momenta originates from relativistic squeezing for the transversal fields which gives a logarithmic increase. For lower momenta the β^{-2} dependence caused by the increased time the particle has for interaction with the material increases the energy loss.

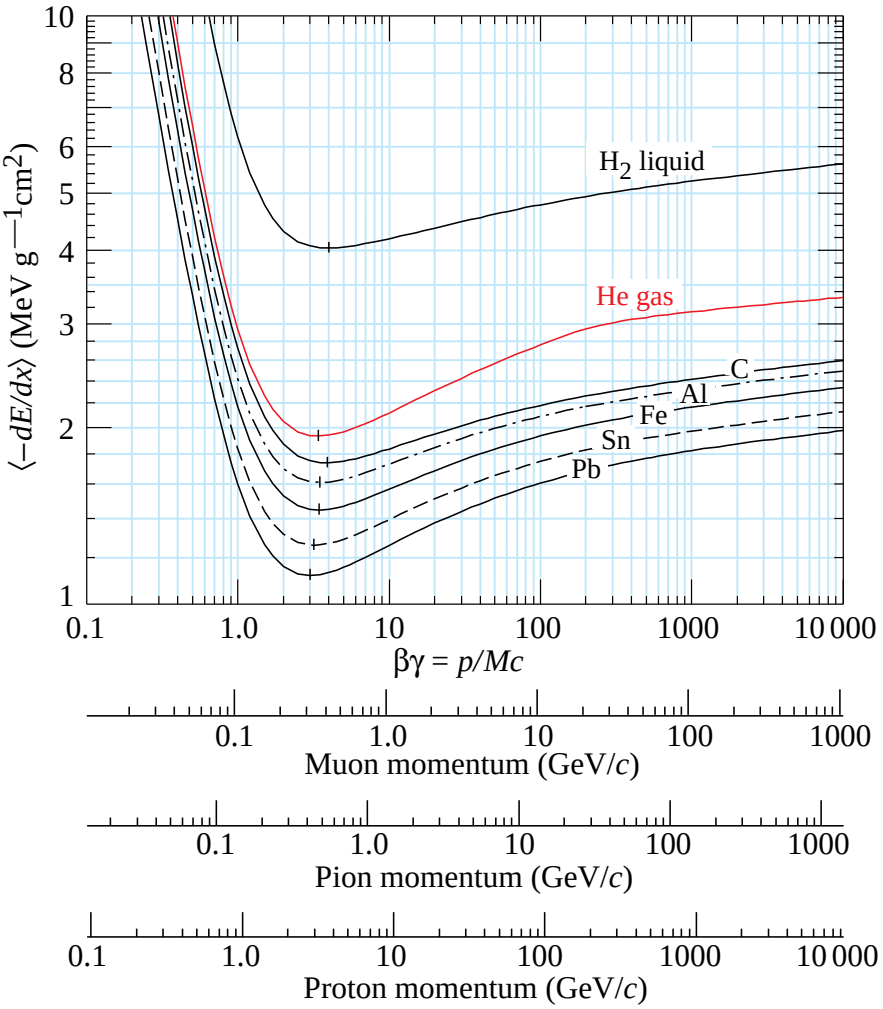

Figure 4.1: Mean energy loss of heavy particles described by the Bethe-Bloch formula for different materials [8].

4.1.2 Electrons and positrons

As electrons and positrons are very light, the contribution of bremsstrahlung becomes significant. The energy loss through ionization for electrons and positrons is described by the Berger-Seltzer-formular [15] seen in Eq. 4.2.

$$-\left\langle \frac{dE}{dx} \right\rangle = \rho \frac{0.153536}{\beta^2} \frac{Z}{A} \cdot \left(B_0(T) - 2\log(\frac{I}{m_e c^2}) - \delta \right) \tag{4.2}$$

- the momentum dependent stopping power $B_0(T)$ of the material
- the density correction δ
- the mean excitation energy I of the material
- the ratio of protons to nucleons of the material $\frac{Z}{A}$
- and the material density ρ

The average energy loss for positrons and electrons in silicon is shown in Fig. 4.1.2. The difference in energy loss between electrons and positrons comes from the fact that electrons from the material and incident electrons are indistinguishable from each other which causes the incident electrons to be repelled more.

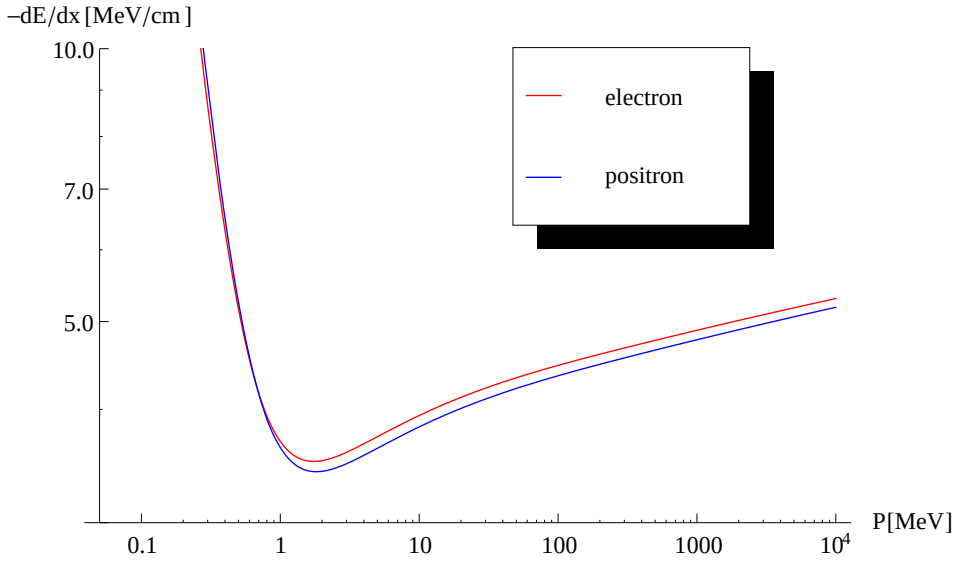

Figure 4.2: Mean energy loss of electrons and positrons in silicon for from 50 keV to 10 GeV. Taken from [16] and drawn from data from [15].

The bremsstrahlungs contribution for relativistic particles ($\beta \approx 1$) [17] is given by Eq. 4.3. It rises with the energy E of the incident particle and depends on the radiation length X_0 of the material.

$$-\frac{dE}{dx} = -\frac{E}{X_0} \tag{4.3}$$

The radiation length of a material depends on the number of protons Z and the number of nucleons A and can be calculated according to Eq. 4.4:

$$X_0 = \frac{716,4\ \mathrm{g/cm^2} \cdot A}{Z(Z+1) \cdot \log(287/\sqrt{Z})} \tag{4.4}$$

4.2 Multiple Coulomb Scattering

When a particle enters a material it won't only scatter one time but multiple times with small angles as seen in Fig. 4.2. The majority of these scatters are caused by the interaction with the Coulomb field of nuclei. A Gaussian approximation for the central 98% of the angular distribution yields Eq. 4.5 [8].

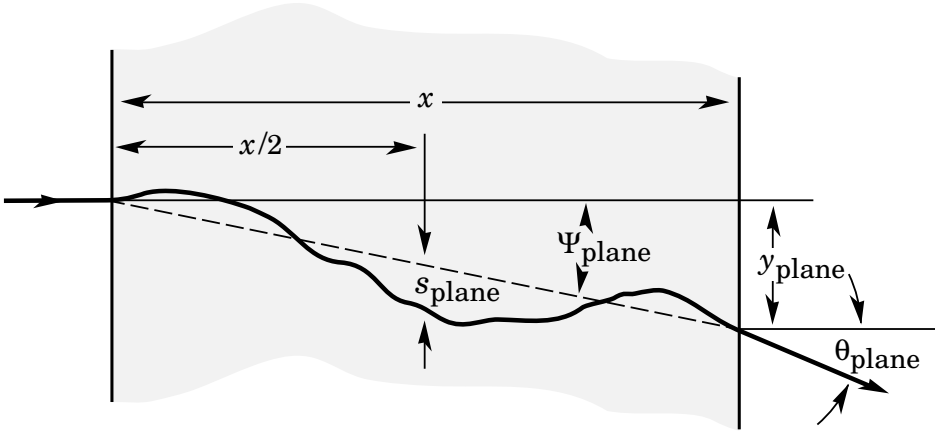

Figure 4.3: Drawing of a particle entering a material and scattering multiple times [8].

$$\Theta_{rms} = \frac{13.6\ \mathrm{MeV}}{\beta cp}\ z\sqrt{\frac{x}{X_0}}\left[1 + 0.038\log\left(\frac{x}{X_0}\right)\right] \tag{4.5}$$

Because the multiple scattering angle Θ_{rms} is inverse proportional to both velocity βc and the momentum p of the particle, a large angle is expected for low momenta particles as the final state electrons in the Mu3e experiment. To counter this dependency, the material budget in terms of radiation length, the so called effective radiation length, x/X_0 has to as low as possible.

4.3 Particle Detectors

To measure the different properties of particles, multiple detector concepts cam be employed to get the most information on the particle. Because the particle has to interact with the detector, the particle will be influenced. This separates detector concepts in two approaches. Minimal interaction detectors try to disturb the particle as little as possible so they need to have as little effective radiation length as possible. Gas tracking detectors and particle identification detectors (PID) using Čherenkov radiation are only two examples for minimal interaction detectors. The second approach is full absorption and is used e.g. for energy measurements in calorimeters. The particle is stopped in a thick layer of high Z material so that its energy is completely absorbed by the detector and measured.
The later approach is not suitable for the Mu3e experiment, as good momentum and vertex resolution are vital to distinguish the signal decay from background. This leaves either thin solid state detectors for tracking or a Time Projection Chamber (TPC) as options.
A TPC consists of a vessel filled with a gas mixture. Sensors are placed on two opposite sides of the frame and a high voltage is applied between both sides. When a particle traverses the TPC it ionizes the gas along its path, creating free ions and electrons in the process. These electrons and ions then drift to one of the charged planes depending on the polarity. The rather constant drift velocity allows for a time resolved track reconstruction. This technique however is quite slow due to the long drift time and is heavily limited in its rate because the gas needs to be discharged for the next particle track or the resolution is corrupted by the charged remnants of the older track. The handling and aging of these detector systems are also problems that make the TPC concept unattractive for Mu3e.
Solid state detectors on the other hand have high rate capabilities and good spacial and time resolution on the price of high material and monetary budget. Semiconductor sensors also use the principle of measuring the ionization of the traversing particle as they create electron-hole-pairs. The late increased demand for semiconductors in the industry has decreased the costs for fabrication of such sensors and thinning processes are industrial standardized now which allows for even thinner sensors for a moderate price.

5 Semiconductor Physics

Silicon and germanium are the most common semiconductors used for sensors. For the Mu3e experiment silicon has been chosen as material, so in the following only the properties of silicon are discussed.

5.1 Silicon

Silicon atoms form a diamond like crystal when condensing into a solid state. Each of its 4 valence electrons forming a covalent bond with its neighbor. A table of important properties of silicon can be found in Tab. 12.2.
Because the energy difference between the bound electrons, the valence band, and unbound states,the conduction band. The conduction band is small in this state, thermally excited electrons can transition from the valence band into the conduction band and act as free charge carriers in the lattice. Such an electron leaves a "hole" behind that can be filled by valence electron from a neighboring atom. This can be treated as a free positive charge. Holes can also be filled by excited electrons recombining in a neutral state.

5.2 Doping

The density free charge carries through thermal excitation are only very few compared to density of atoms. To increase the number of charge carriers impurities are artificially implanted in the crystal which is called doping. These impurities are atoms with 3 or 5 valence electrons like Boron or Phosphorous which produce free additional holes or electrons in the crystal. Implants that produce electrons are called donators and produce a crystal with more free negative charge carriers, a n-doped substrate. Analog, implants that produce holes are referred to as acceptors which create a p-doped substrate.

5.3 P-N-junction Diode

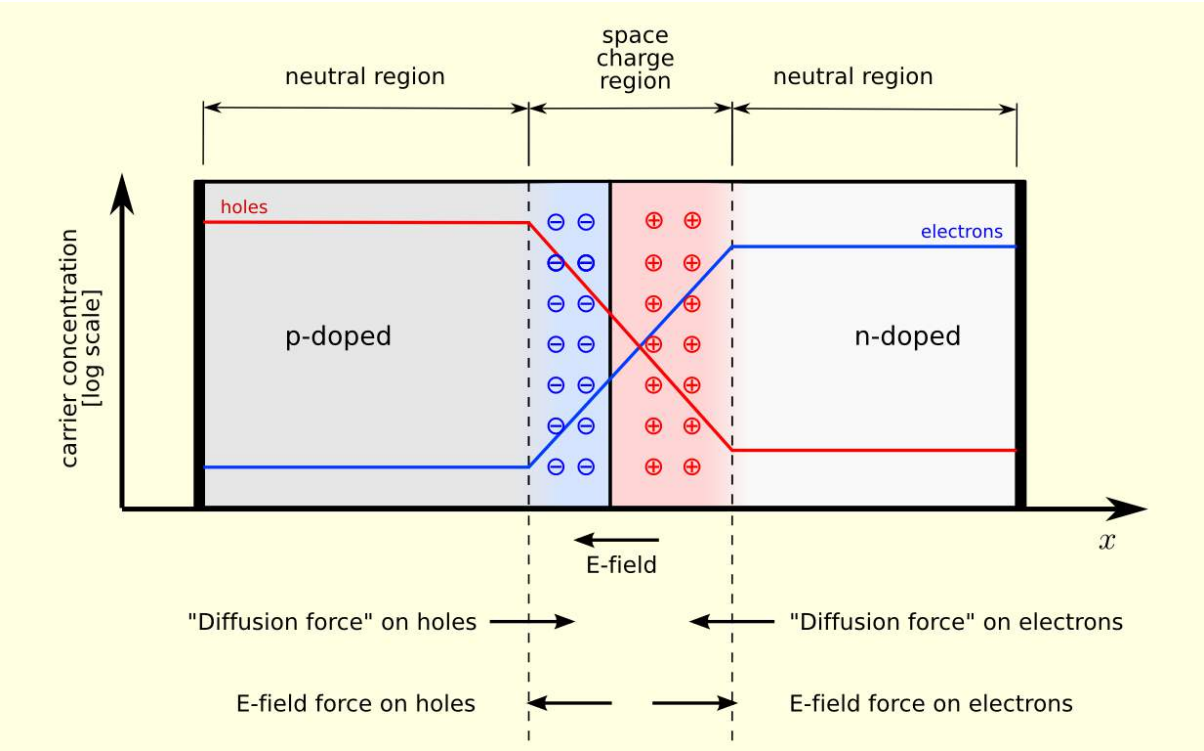

Figure 5.1: Illustration of the PN-junction equilibrium from [18]

The boundary between a n-doped and a p-doped substrate is called pn-junction which can be used as diode. At this contact, the difference in concentration of free charge carriers is large so that they start to diffuse into the other doped region and recombine with each other. This leaves the implant atoms as ions, which creates an electric field at the junction. This field creates a drift opposed to the diffusion. At the equilibrium point, the diffusion and the drift due to the field balance out and create a region with no free charge carriers called the depletion zone (Fig. 5.1).
With that assumption one gets for the diffusion voltage of the junction:

$$U_D = U_T \cdot \log(\frac{N_A N_D}{n_i^2}) \tag{5.1}$$

Given:

- U_T the thermal voltage equivalent
- N_i the doping concentration of acceptors and donators
- n_i the intrinsic charge carrier concentration

Using $E = \frac{dU}{dx}$ one gets the Poisson equation for this system:

$$\frac{d^2U(x)}{dx^2} = -\frac{\rho(x)}{\epsilon_0 \epsilon} \tag{5.2}$$

With the charge carrier concentrations $\rho(x)$, the dielectric constant ϵ_0 and the relative permittivity ϵ. Solving this equation as described in [16] yields the following equation for the width of the depletion zone w:

$$w = \sqrt{\frac{2\epsilon_0 \epsilon U_0}{e} \frac{N_A + N_D}{N_A \cdot N_D}} \tag{5.3}$$

Which was estimated to $\approx 8\mu m$ at $-60V$ HV in [16], growing to $\approx 10\mu m$ at higher voltages. Taking the energy deposition of the final state particles in silicon (Fig. 4.1.2) into account, a mean energy deposition per particle of $\approx 4keV$ in the depletion zone is expected.

5.4 Charge Collection

When a charged particle passes through a semiconductor, it will excite electrons from the valence band to the conduction band of the crystal as described in section 4 which creates electron-hole pairs. Low energy photons however will be absorbed via the photoelectric effect. This process creates one free electron with enough energy to create secondary electron-hole pairs, resulting in a charge cloud.
The charge collection in a diode can be divided in two components. The drift process is governed by the strength of the electric field E as charge carries are attracted by the electric field. This effect is fast and depends on the mobility μ of the substrate. Charge carriers outside the depletion zone diffuse and will most probably recombine. Some free charge carries diffuse in the depletion zone but those charge carriers will most likely be negligible compared to the primary drift charges.
This results in an average drift velocity:

$$v_{drift} = E \cdot \mu \tag{5.4}$$

6 Pixeldetectors and HV-MAPS

6.1 Pixel Detectors

Semiconductor pixels sensors are nowadays commonly used in particle physics experiments such as ATLAS and CMS at LHC. These sensors provide high granularity and rate capability while being relatively radiation hard. They are typically produced with lithographic processes applied to a silicon or germanium wafer. With the doping from the lithography, the resulting substrate can be used as detection diode and can be fully depleted. To read them out, an additional sensor is needed which is bump bonded on the doped substrate. This process however is complicated and expensive. The additional material in the flight path of the particles increases the effective radiation length also significantly.
Because radiation length and the induced multiple scattering are a hard constraint for the Mu3e experiment, a chip technology with an integrated readout is suited best for the experiment. The HV-MAPS technology combines fast charge collection with an integrated readout and was found to be the best suitable technology.

6.2 Monolithic Active Pixel Sensors (MAPS)

Active Pixel Sensors (APS) where fist developed by the photo industry, and split the pixel into a sensitive part and a digital readout part. These structures could only make use of the surface as sensitive area which lead to a rather small form factor of $\approx 30\%$. This constraint does not apply for particle detectors so technically the whole substrate can be used as sensor volume with the readout electronics on the surface. This design is called Monolithic Active Pixel Sensor (MAPS). MAPS have been developed since the 90s and can be produced in commercial Very Large Scale Integrated (VLSI) CMOS processes which allows to produce these sensors in large numbers and at low costs. Applications for MAPS are currently e.g. the STAR vertex detector [19] or the EUDET beam telescopes [20], which both use the MIMOSA [19] chip. These chips however do not deplete the substrate, so charge is collected via diffusion. Because they rely on diffusion MAPS are usually slower and produce smaller signals than depleted designs which rely on drift.

6.3 High Voltage Monolithic Active Pixel Sensor (HV-MAPS

HV-MAPS combine the concept of depleted detection diodes with the MAPS concept. A HV-MAPS pixel consist of a deep n-well inside of a p-doped substrate. The n-well houses the pixel logic as seen in Fig. 6.1. The p-n-junction serves as diode which is depleted by a high reverse bias voltage (HV). This allows for fast charge collection and form factor of almost 100% at the same time. These designs can be produced with High Voltage CMOS (HV-CMOS) processes which are industrial standards for e.g. the automobile or power industry.
Because the depletion zone is only $\approx 10\mu m$ thick, the chip can be thinned industrially to $50\mu m$ thickness.
The HV-MAPS concept was first proposed by Ivan Perić in 2006 [21] and was adapted by him for use in the Mu3e experiment.

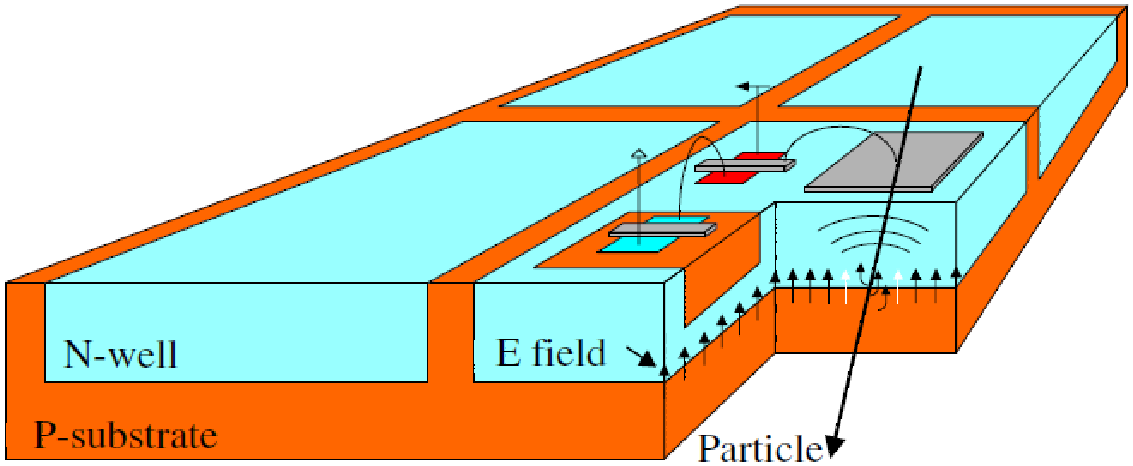

Figure 6.1: Simplified HV-MAPS pixel concept [21]

Part II

Setup

7 The MuPix

The MuPixel or short MuPix chips are a series of HV-MAPS prototypes for the Mu3e experiment. For this thesis only the MuPix4 and MuPix6 have been studied intensively but a few consistency measurements for the MuPix7, the newest prototype, are also presented in this thesis.

7.1 MuPix4

The MuPix4 was studied in detail in [22]. It has an error in the readout scheme which causes some of the address RAM-cells to be reset before they are readout completely. As consequence only every second double row of pixels can be read out digitally and the other pixels are projected to the bottom double row. This pattern is called "Strixel-pattern" (Fig. 7.1). The chip itself is a 250µm thick and $3.5 \times 4.16\text{mm}^2$ large silicon chip. It houses a 32×40 pixels matrix with a column pitch of 92µm and a row pitch of 80µm. The ratio of area occupied by the digital part to the sensitive area is $\approx 11\%$. Each pixel consists of a 3×3 diode structure (Fig. 7.3) in which the charge sensitive amplifier (CSA) is placed in the deep n-well of the central diode. A source follower (SF) drives the signal to it's digital counterpart in the periphery where it's discriminated and digitalized.

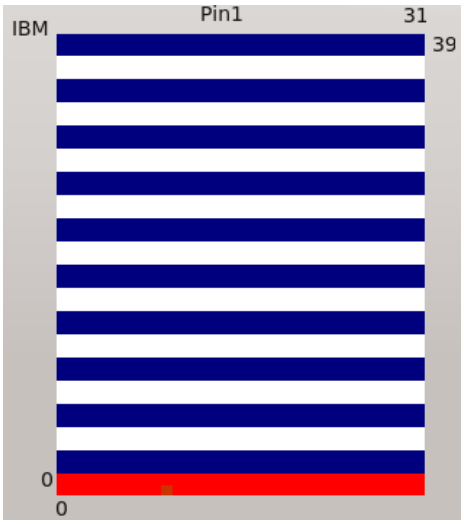

Figure 7.1: The "strixel" pattern of the MuPix4 prototype observed with the online monitor taken from [16].

7.2 Mupix6

7.2.1 Layout

The MuPix6 is actually the fifth MuPix generation and was designed to fix the issues with the MuPix4 and test a new amplification concept in the periphery to separate signal pulses better from noise and digital cross-talk.
The chip has almost the same geometry as his predecessor. The pixel size was changed to $102 \times 80 \mu m^2$ but the fraction of digital to sensitive area is the same. This is grow in width is due to the additional amplification stage in the digital part which takes up more space. The pixel had to be larger in turn to keep the digital and sensitive parts aligned. In Fig. 7.3 both the sensitive pixel and the corresponding digital part are shown on scale. The digital pixels are arranged in a 64×20 matrix instead of the the 32×40 matrix of the pixels. Each column of pixels corresponds to 2 columns in the digital part which means that the read out address has to be converted as only the digital address is transmitted. The decoding procedure can be found in [23] for MuPix4 and for MuPix6 in [24].
The first 4 physical columns of the MuPix6 were designed without the second amplification stage to compare the effects of the second amplification stage to the MuPix4-like design without the second stage. This layout can be seen in Fig. 7.2. These pixels are akin to the MuPix4 pixels but are not identical because, e.g, all pixels on the MuPix6 chip pixels, ones with 1 amplification stage or ones with 2, share a new comparator design which is different from the MuPix4 design.
Aside from the digital and analog pixels, the chip also has 2 shift registers for configuration. One controls the bias voltages for the global DACs (Section 7.2.3) and the other one stores the "Tune-DACs" and "Hitbus" information which is explained in the following section.

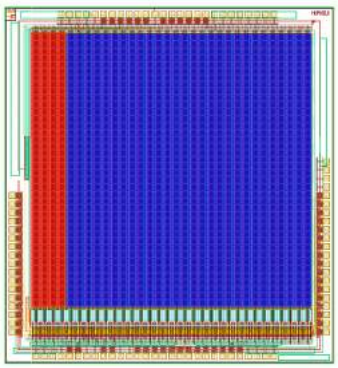

Figure 7.2: The MuPix6 Chip Layout exported from Cadence® Red: 1-staged pixel, blue: 2-staged pixel.

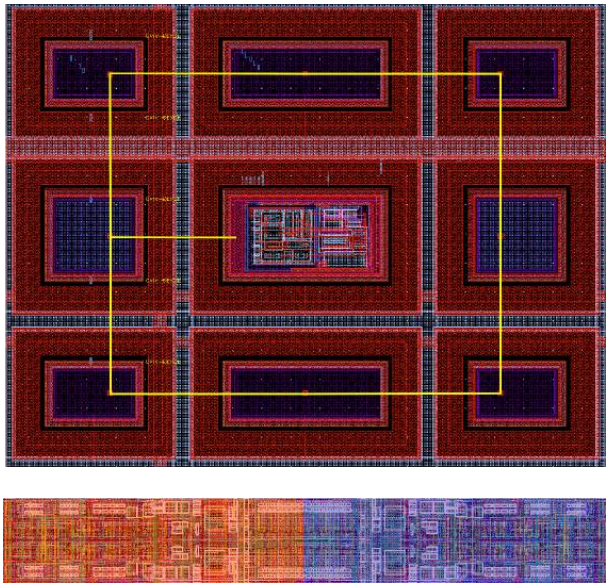

Figure 7.3: The MuPix6 Pixel Layout exported from Cadence®. Scaling is identical for both parts. Taken from [16]

7.2.2 Design

Fig. 7.5 shows the simplified circuitry of the analog component of the pixel.
The part shown in the top is located in the physical pixel while the part shown on the bottom is housed in the periphery. A list of all the bias voltages and their effect and location is complied in Tab. 7.1.
In the first stage the reverse biased diode of the pixel generates a pulse which is amplified by the CSA. A diode testpulse can also be created artificially via an externally applied voltage, which charges a capacity which is released on command. This so called injection is split into injection1 and injection2 so that injection1 only controls every first pair of physical rows and injection2 every second pair. The pattern looks like the "Strixel" pattern of the MuPix4 [7.1] with injection1 supplying the pixels who cant be read out digitally and injection2 supplying the ones that can be read out. Fig. 7.4 shows how an injectioin is generated. The external voltage charges the capacity between the two metal layers which in turn draw electrons out of the n-well and release them back once the external voltage is released.
VN provides the current for the CSA while VNLoad and VPCasc steer the shaping and amplification. VNFB provides a linear feedback. As the CSA can not drive the pulse from the sensitive region to the periphery, the SF which is controlled by VNFoll is needed.
In the second stage the function of the bias voltages are identical to their namesakes in the first stage.

Both amplification stages can be adjusted independent from each other so that additional biases are necessary. The output of the second CSA is then coupled capacitively to the external baseline (BL) which is the input voltage of the comparator. The baseline restoration (BlRes) works as resistor and steers how fast the voltage level is restored to the external level.
The threshold (THR) is the level the modulated baseline has to surpass for the comparator to create a pulse. The threshold is additionally fine tune-able via a 4-Bit tune DAC (TDAC). The tune DACs allow to compensate for inhomogeneities between the pixels which can occur due to the production process. This allows to scale down noisier pixels and have a more homogeneous response of the chip. The range of the tune DACs is dynamic in that they are supplied by global voltage (VPDAC) which then is scaled by the tune DAC of the pixel.
If the comparator has generated a pulse, an edge detector controlled by VNDel triggers a hit latch which stores a flag until it's readout and reset.
The Hitbus allows to look at the comparator output of a selected pixel. It can only be enabled for one pixel at a time but is configurable in one of the shift registers. With this output it's possible to measure the Time-over-Threshold (ToT), the time during which the pulse is higher than the threshold and the comparator is generating a pulse. Although the pulse of the MuPix4 is positive and the pulse of the MuPix6 is negative compared to the baseline, the comparator output is called ToT. It is inverted for positive pulses so that the results are comparable.
Because the second amplification stage also inverts the pulse, the pixel with only one stage can only be operated at a threshold higher than the baseline while the pixel with 2 stages can only be operated at thresholds lower than the baseline.

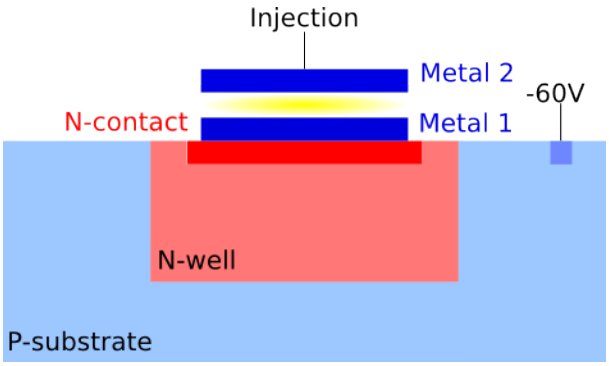

Figure 7.4: Schematic drawing of detection electrode. Metal layer 1 is the the detection electrode which is either charged by the injection from metal layer 2 or from the N-contact.

Bias Voltage	Origin	Circuit Part	Function	Effect
VN	DAC	CSA	Current Source	On/Off switch steers current
VNLoad	DAC	CSA	Voltage divider	adjusts amplification
VPCasc	External	CSA		
VNFB	DAC	CSA	Resistance	linear CSA feedback
VNFoll	DAC	SF	Current source	SF output voltage control
VN2	DAC	Amp2	Current Source	On/Off switch steers current
VNLoad2	DAC	Amp2	Voltage divider	adjusts amplification
VPCasc	External	Amp2		
VNFB2	DAC	Amp2	Resistance	linear CSA feedback
VPComp	DAC	Comparator	Current source	Current & speed control On/Off switch
BL	External	Comparator	Baseline	Voltage offset for signal Comparator input
THR	External	Comparator	Threshold	Comparator reference
BLRes	DAC	Comparator	Resitance	Shaping
VPDAC	DAC	Comparator		Tuning
VNDel	DAC	Edge detector		Delay

Table 7.1: Summary of the bias voltages taken from [16]

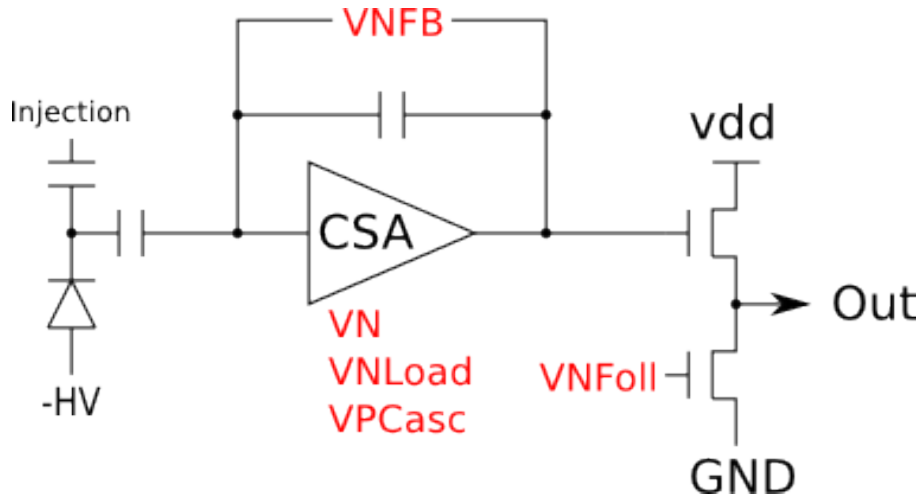

(a) Simplified schematic of the in-pixel logic. "Out" is the line to the periphery.

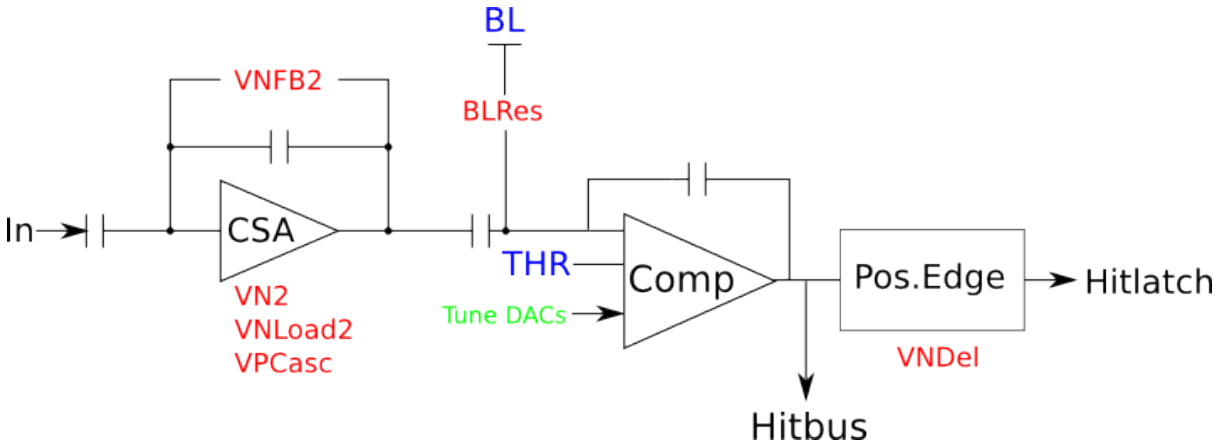

(b) The comparator electronics. "In" is the line from the pixel.

Figure 7.5: Schematics of the analog parts of the MuPix6 pixel. Bias voltages are written in red, external voltages in blue. Taken from [16].

7.2.3 Shaping

Pulse shaping describes the development of the pulse form the primary signal at the detection electrode to its final from before the comparator. The shaping for older MuPix prototypes has been discussed in [25] and [26], based on [27].
To describe the pulseshape of the MuPix a few approximations are made. As fist step, the input signal from the detection electrode in the CSA is a rectangular function, meaning it $U(t) = 1 \ \forall \ t \in (0, a)$ and 0 otherwise. The high-pass behavior of the circuit can be approximated as a CR-filter or differentiator and the low-pass behavior can be simplified to a RC-filter or integrator. The resulting pulse is then the convolution of those functions (Eq. 7.1).

$$U_{final}(t) = U_{electrode}(t) * U_{CR}(t) * U_{RC}(t) \tag{7.1}$$

The solutions for the filters are:

$$U_{CR}(t) = U_0 \cdot e^{-t/\tau_{diff}} \tag{7.2}$$

$$U_{RC}(t) = U_0 \cdot (1 - e^{-t/\tau_{int}}) \tag{7.3}$$

For the convoluted pulse one gets 2 solutions depending on the time constants τ_i of the filters:

$$U_{pulse}(t) = U_0 \frac{\tau_{int}}{\tau_{int} - \tau_{diff}} (e^{-t/\tau_{int}} - e^{-t/\tau_{diff}}) \text{ for } \tau_{int} > \tau_{diff} \tag{7.4}$$

$$U_{pulse}(t) = U_0 \cdot \frac{t}{\tau} \cdot e^{-t/\tau} \text{ for } \tau_{diff} = \tau_{int} = \tau \tag{7.5}$$

Fig. 7.6 shows pulseshapes for different time constants. It shows that a longer time constant in the high-pass filter prolongs the pulse heavily while also flattening the top. For for high pulses compared to the threhsold, the latency is small compared to ToT so that the differentiator can be neglected. The resulting pulse length can be approximated by the inverse of the pulseshape function, which results in a logarithmic behavior depending on the initially deposited charge:

$$t_{ToT} \approx \tau_{int} \cdot log(U_0) \tag{7.6}$$

This approximation doesn't take the linear feedback into account but is still reasonable for the MuPix4. In the case of the MuPix6 this approximation gets worse as the pulse is shaped again, resulting in the convolution of two pulseshapings. However it is still a good assumption to gauge the dependence of the shaping.
The full path of pulse is drawn in Fig. 7.7.

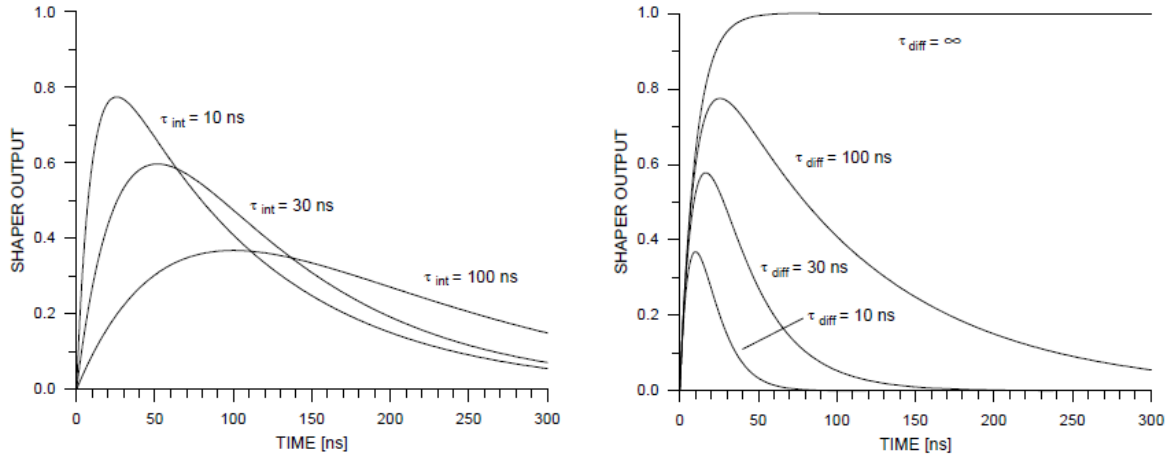

Figure 7.6: Pulseshapes with various time constants. τ_{int} = 100ns for the left drawing and τ_{diff} = 10ns for the right drawing. Extracted from [27].

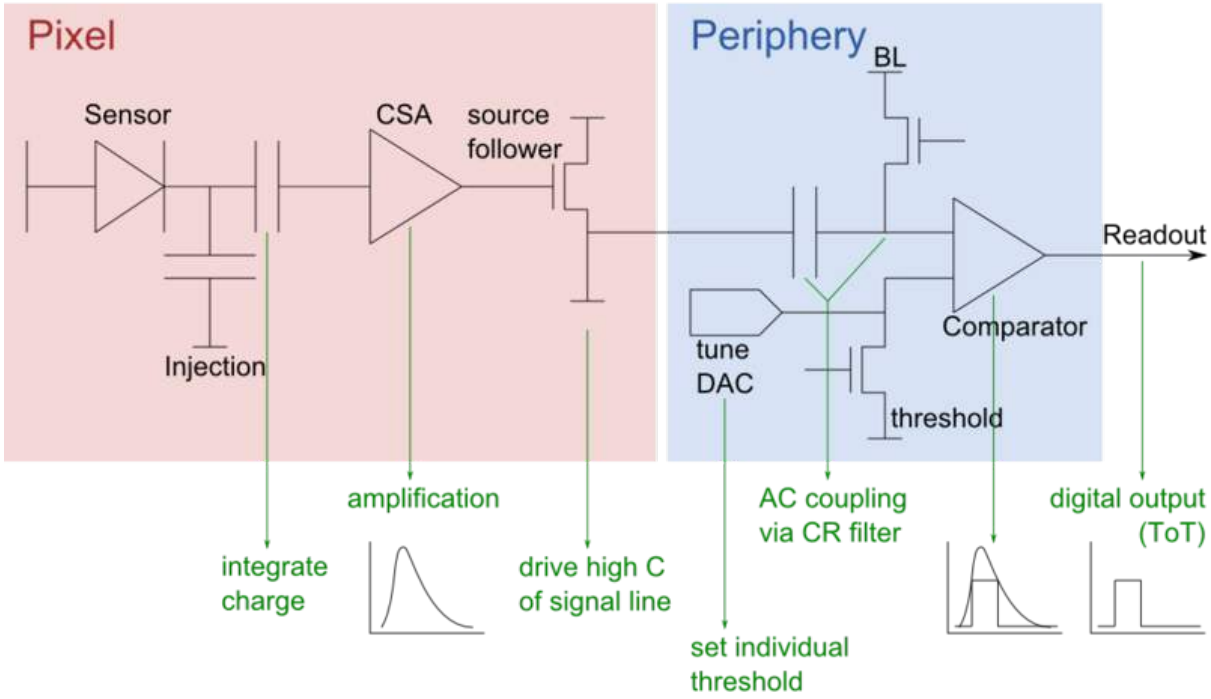

Figure 7.7: Drawing of the pixel and periphery of a MuPix4 and their effect on the pulse. From [25]

7.3 MuPix7

The MuPix7 is the newest MuPix prototype. The analog part and the sensitive region are identical to the MuPix6 aside from a sight change in the HV distribution. The innovation lies in the digital part as it has a fully integrated state machine and a Gbit/s serial readout. The MuPix7 also generates its own time stamps. Furthermore, the MuPix7 can also be operated in MuPix6 mode, meaning that the state machine is provided externally by the external software and not the chip itself and the parallel readout is used. This operation mode was used for the MuPix7 results presented in this thesis. So far, the first test results show promise but further tests are required.

8 Test Setup

8.1 Readout and Hardware

Both MuPix4 and 6 are each read out parallel via an external state machine run on an Field Programmable Gate Array (FPGA). The scheme and FPGA software are explained in detail in [16].
The chip itself is glued and wire bonded onto the MuPix test board (Fig. 8.1) designed by Dirk Wiedner [28] or glued and bonded to a carrier package which is placed in a socket soldered to the socket pins in the center of the PCB. This Printed Circuit Board (PCB) supplies the voltages necessary for operating the chip and and acts as an interface for communication between the FPGA and the chip.
The configuration of chip and board, the so called "slow control", is done via a 40 pole flat ribbon cable which is connected to the FPGA via an adapter card. The output data was originally read out via another 40 pin ribbon cable which proved to be very susceptible to cross-talk between the address and time-stamp bit lines [22] and was replaced by a Low Voltage Differential Signal (LVDS) transmission.
The LVDS adapter card, both board and FPGA side, and the Slow Control adapter card were also designed by Dirk Wiedner. The hitbus signal is also connected to the LVDS card as it induced cross-talk and was in turn influenced by cross-talk. The FPGA side adapter cards are connected to the FPGA via the 2 High Speed Mezzanine Card Connectors (HSMC) of the Stratix IV FPGA card which is used for the setup. The Stratix board is in turn connected to a computer via a PCI-E slot.
The setup containing the chip, PCB, adapter cards, FPGA and computer is referred to as the "single setup" (Fig. 8.2) and is used for characterizing the MuPix prototypes. It's also the setup used for the measurements in this thesis.
The other MuPix test setup, the "MuPix Telescope" [24], contains 4 MuPix boards connected to 2 FPGAs and is used for integration and efficiency studies. It's is not topic of this thesis.

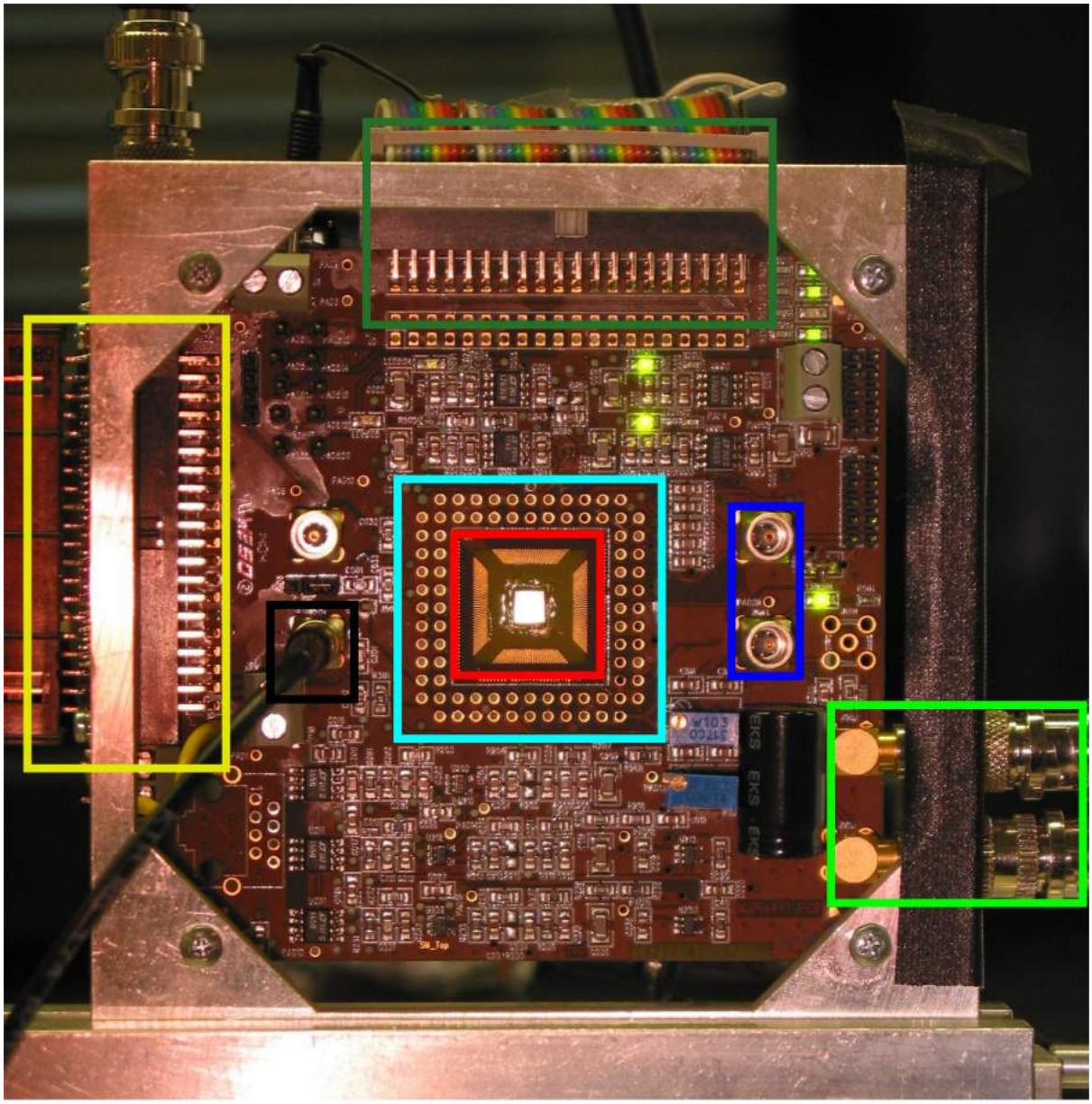

Figure 8.1: MuPix PCB. Light Green: Power input for low voltage on top and HV on the bottom. Black: Hitbus connected to the LVDS adapter card. Blue: injection 1 on top and 2 on the bottom. Yellow: Data output which is connected to the LVDS adapter board. Dark Green: Slow Control connector. Cyan: Carrier Socket Connectors/Test Points. Red: MuPix Chip.

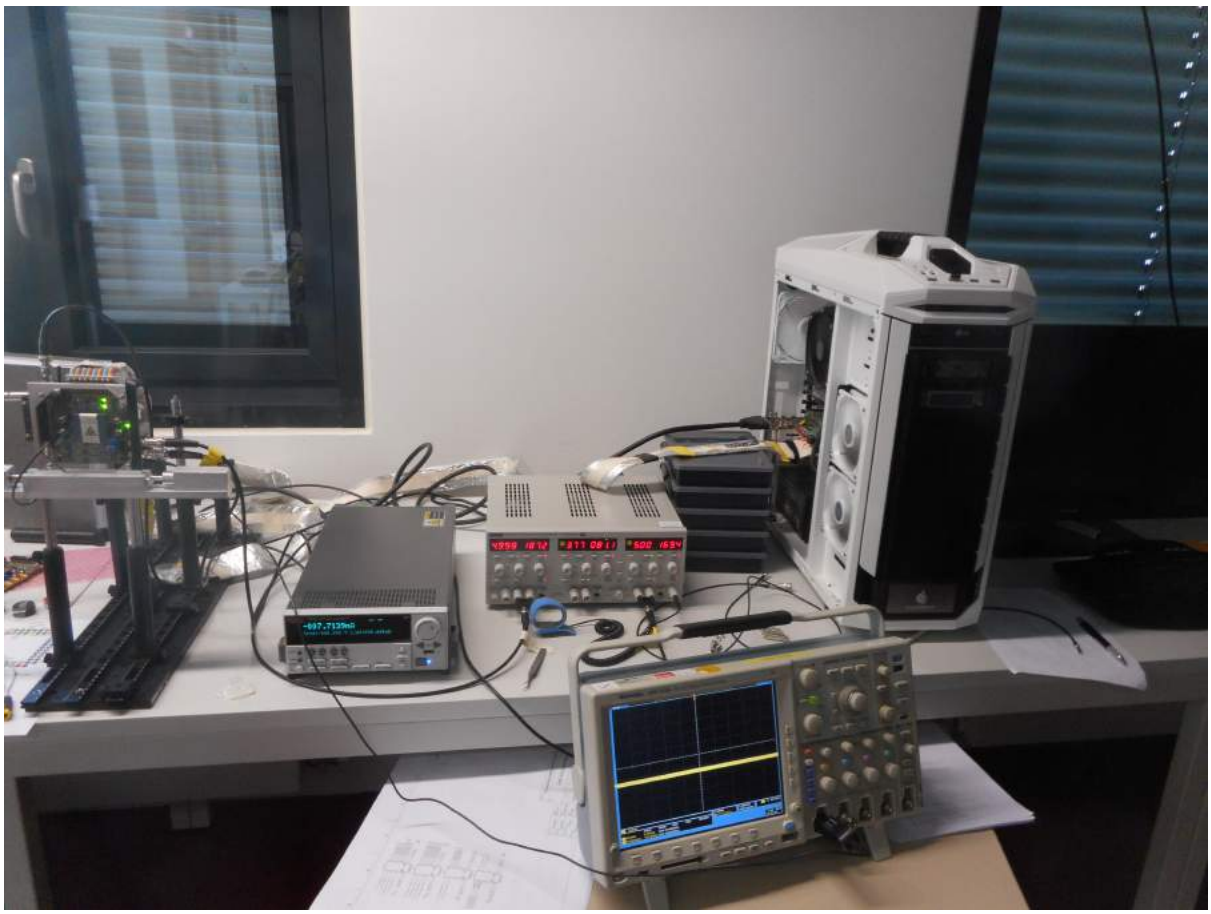

Figure 8.2: Single setup. From left to right: MuPix PCB in a custom metal frame with the iron source covering the chip, the power supply for the HV [29], the power supply for the low voltage [30] to power the chip and PCB, oscilloscope and the computer housing the FPGA.

8.2 Software

8.2.1 FPGA Firmware

The firmware on the FPGA controls the state machine and provides an interface for communication between the computer and the MuPix. The data read from the MuPix is stored in the memory of the FPGA which processes and saves the data, which is then mapped into the memory of the computer [31]. A specialized driver had to be written in order for the FPGA and the computer to transfer the data properly [32].
One of the main feature of the FPGA is the 48-bit clock that increments with 400MHz frequency. This clock governs the timing of the readout of the data acquisition as seen in Fig. 8.3.
8 bits of the clock are send as timestamps to the chip as it can not generate its own timing information. These fine counter bits can be moved via a division factor to slow down the timing artificially. Each increment of the division factor corresponds to a division of the clock frequency by 2. The timestamps sent to the chip are also Gray-encoded [33] to minimize cross talk as only 1 bit changes per increment. The rest of of the clock bits constitute the coarse counter which is added by the FPGA to have unique time stamps during extended periods of data acquisition.

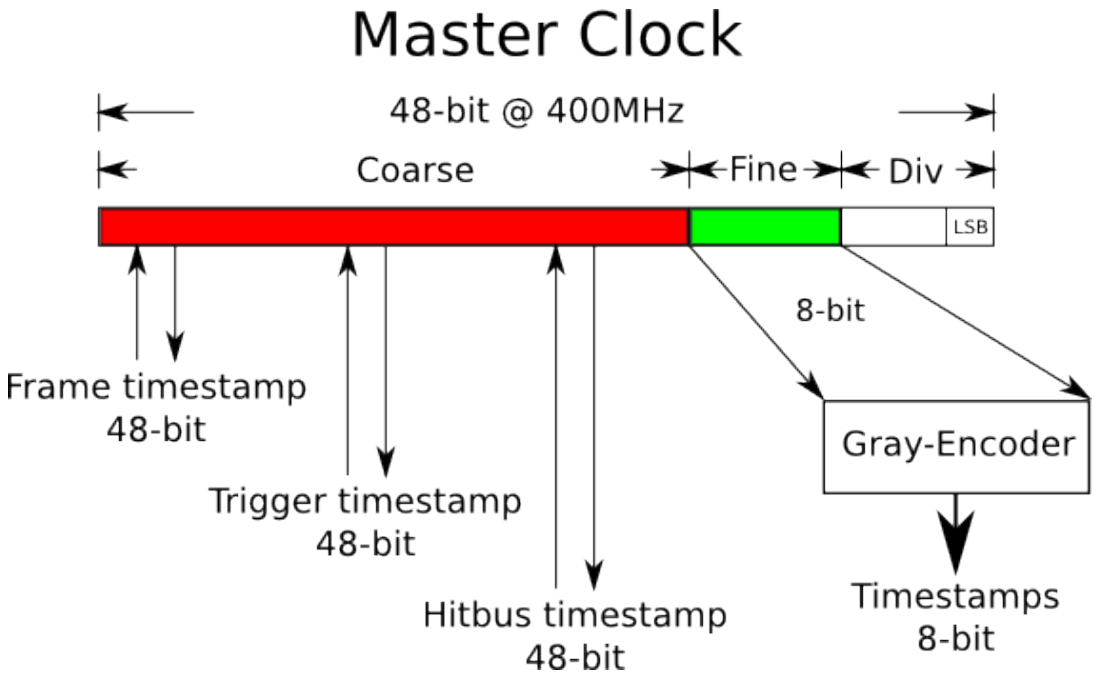

Figure 8.3: Main timing scheme of the FPGA: Division factor (Div), Coarse Time information and Fine time provided by the timestamps

This clock is also used for sampling trigger information which can be added to the readout via an input on the FPGA-side LVDS-adapter board. This procedure has been modified to sample the hitbus signal and save the data in a histogram of 1024 bins of 4ns so that the ToT information can be stored and evaluated digitally.
Aside from timing information the FPGA also controls the DACs on the PCB for the threshold and for the injections as well as the shift registers of the chip.

8.2.2 GUI

The Graphical User Interface (GUI) allows configuring the MuPix and FPGA from the computer side by hand. It is based on the MuPix software ([24] and [16]).This software framework is used for both the single setup and the MuPix Telescope [24]. It's written in C++ and makes use of Qt- [34] and boost-libraries [35]. Fig. 8.4 shows the layout of the GUI. The colored parts provide different functionalities explained in the following:

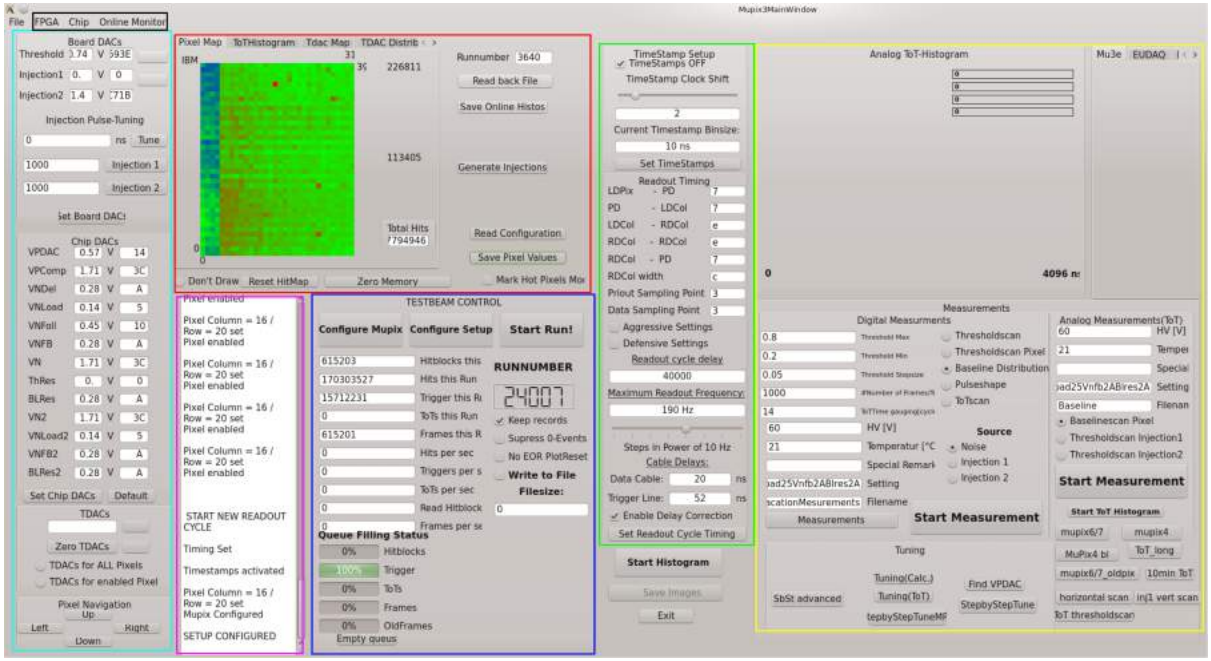

Figure 8.4: Interface window of the MuPix software. Coloring is explained in section 8.2.2

Maps and histograms - here are the maps and distributions of the current run of data acquisition and configuration displayed. The Pixel Map shows the number of hits in each pixel since the start of the run color scaled to the most hits in a pixel. Other maps include the map of the TDAC values or the measured noise levels of the pixels.

Testbeam Control - in this part are the buttons to configure the chip and to start/stop a run located. This allows for extended periods of data taking which is used e.g. for testbeam campaigns , hence the name. The current status of the different data queues as well as the rates and total numbers for the current run are also displayed.

Timing Control - this part controls the timing of the readout state machine. The Clock Shift is the division factor of the master clock (Fig. 8.3). The readout timing controls the delay between the different states of the readout cycle in hexadecimal units of the master clock. The readout cycle delay governs the readout frequency, which is the time the FPGA waits between starting readout cycles. Additionally a delay correction for time alignment between trigger and MuPix data is implemented.

DAC Control - here the user can configure the on-board DACs of the PCB and the DACs which are written in the shift register of the chip. The threshold and the injection voltages can be set in mV and are then converted to the corresponding value for the DAC. The chip DACs are usually set in hexadecimal numbers from 0x0 to 0x3F which is the range of a 6 bit DAC. Additionally the TDACs of all or the enabled pixels can be set or reset here manually.

Additional Windows - these tabs allow to check the FPGAs memory or registers to be checked for errors or bugs. The Online Monitor opens a new window where different correlations between hits and triggers are displayed to check for alignment in time and space and to check for problems with the data acquisition.

Measurements - in this region of the GUI numerous analog and digital measurements are implemented. The top part shows the latest recorded ToT data as a histogram. Analog measurements use the hitbus information while digital measurements usually count the number of hits for different settings. On the bottom right multiple methods for setting the TDACs, the so called "tuning", are implemented.

8.3 X-Ray Setup

To measure the energy resolution of the MuPix chip a X-ray spectroscope by PHYWE [36] from the lab course for medicine students [37] was borrowed. It is designed for experiments with X-rays and their reflection on a crystal lattice. It has a tungsten anode and a LiF crystal mounted at the rotation axis of a goniometer arm. At the end of the arm a Charge-Coupled Device (CCD) camera is used to to count the number of photons which where reflected at the crystal lattice. The cathode voltage of the apparatus can be set between 5 and 35kV to change the energy spectrum of the emitted photons and the current can be set from 0.01 to 1mA to control the intensity.
A special adapter board was made by the workshop of the institute on which the MuPix PCB could be mounted. This adapter board was used instead of the CCD for the lab course experiment. The cable canal in the apparatus proved to be too narrow for all the cables to fit through so the LVDS adapter board was left outside the apparatus. The hitbus was connected to the LVDS board so that analog measurements were still possible.

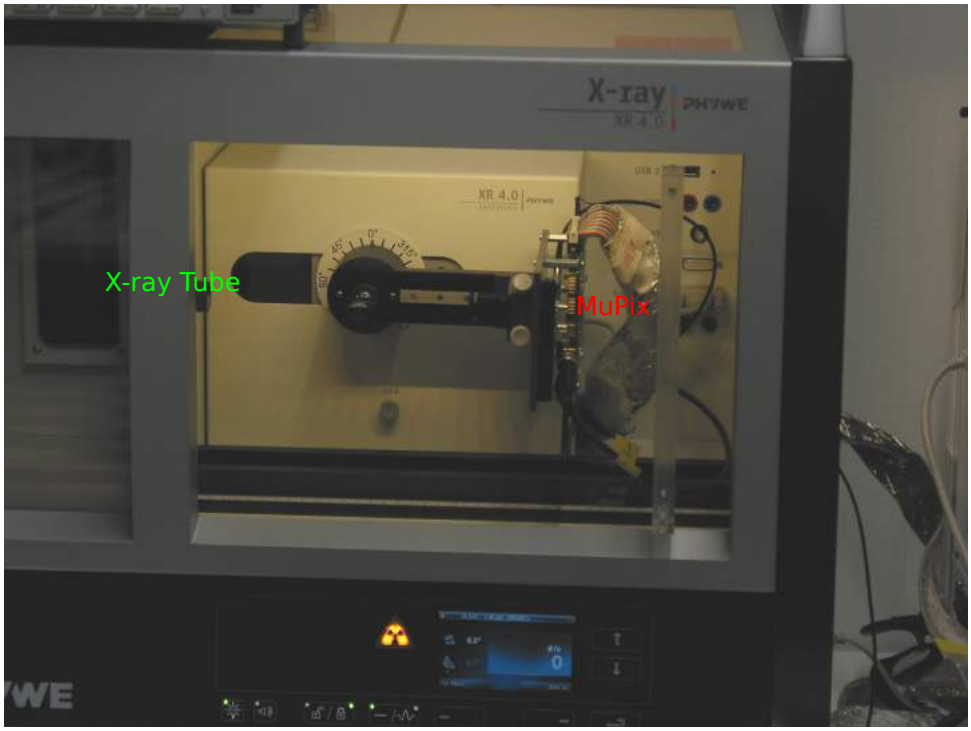

Figure 8.5: The MuPix placed in the X-ray spectroscope [36]

8.4 Climate Chamber

Previously, measurements to gauge the temperature dependency were done in a climate chamber. Because of tension between results, e.g the signal-to-noise-ratio in [16] with a value of $\approx$ 10 to 15 and in [22] with a signal-to-noise-ratio of over 30 , it was suspected that the chamber acted as Faraday cage, shielding the chip. To measure the effect of the shielding, the MuPix PCB was placed in the chamber like in Fig. 8.6.

Figure 8.6: The MuPix PCB with a chip on package in the oven

Part III

Measurements

9 Measurement Methods

In this chapter the methods are described that where used to acquire the data presented in this thesis. The measured data as well as the generation of the signals are discussed.

9.1 Measured Variables

9.1.1 Time over Threshold

As described in 7.2.2 and 8.2.1, the chip can be configured such that the comparator signal is directly send out and stored on the FPGA. Because the hitbus signal is transmitted via LVDS, the signal the FPGA receives is distorted compared to the signal directly measured with an oscilloscope. The difference has been measured in Fig. 9.1 and is a rather constant 60ns. This offset was only measured for long ToTs so it could be smaller for short ToTs. The effect is also described in [16].
Other possibilities are counting the number of pulses induced by a signal. For example, the FPGA can trigger a given amount of injections and count the received pulses to measure the fraction of detected pulses. This can be used to reconstruct the pulse shape by measuring the latency and duration of the comparator response for different thresholds. One should keep in mind that the ToT is dependent on the threshold and on the pulse shape parameters as described in 7.2.3. The hitbus is also only available for 1 pixel at a time.

9.1.2 Digital Hit Information

When reading out the chip digitally the complete pixel matrix is available except the pixels with 1 amplification stage for thresholds lower than the baseline and vice versa as explained in 7.2.2. The digital hit information by itself is only of boolean nature but can be used to measure hit distributions and can be accumulated to acquire statistical information.

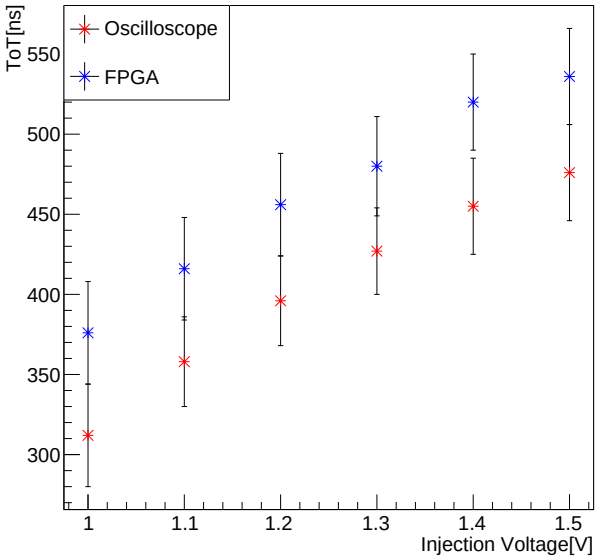

Figure 9.1: ToT measured with an oscilloscope and the FPGA for different injection voltages

9.2 Signal Sources

9.2.1 Injection

As described in 7.2.2 the 2 injection lines allow to release a pulse if a set amount of charge at a configurable time and interval. An external positive voltage causes electrons to be collected at an electrode contact at the n-well which mimics a pulse. The internal capacity of the pixel differs from pixel to pixel as there are large production uncertainties [38].

9.2.2 Iron Source

A radioactive Iron-55 (Fe-55) source was used as a reference signal. When Fe-55 decays to Mn-55 via electron capture a higher shell electron takes the place of the absorbed one and emits a photon of a fixed energy or an Auger electron is emitted. The Auger electron can not leave the probe and can therefore be ignored. The emitted γ originates most of the time from the K_α line which has an energy of 5.9keV. The K_β line at 6.49keV is suppressed compared to the K_α. The photon converts into an electron of the same energy via the photoelectric effect. This 5.9keV electron has a short free mean path length of less than 1 µm [39]. It ionizes other electrons in the substrate and creates electron-hole-pairs which are then collected by the pixel electrodes.

9.2.3 X-Ray Source

As mentioned in 8.3 a X-Ray tube was used to provide γ's of various energies. Electrons are accelerated from the cathode to the anode of the X-ray tube which emits bremsstrahlung photons. The characteristic spectrum contains the discrete lines of the tungsten anode [37].

9.3 Measurement Procedures

9.3.1 ToT Histogram

The histogram function of the FPGA [8.2.1] allows to store the timing information of multiple ToTs [9.1.1]. These histograms allow to measure the mean ToT and the width of the ToT distribution. In this thesis Gauss fits were used, so the mean ToT is the mean of the gaussian and the width of the distribution is the width of the gaussian.

9.3.2 Threshold Scan

The term threshold scan describes the measurement of a signal at different comparator thresholds to get information about the pulse shape. It allows to measure the pulseheight and to reconstruct the shape of the pulse. This measurement can be done either digital or analog. Measuring digitally means that the number of hits per readout cycles is measured for different thresholds. Analog measurements have additional time information as the delay between a triggered injection and a received pulse can be measured. Together with the duration of the pulse this allows to reconstruct the rising and falling edges of the pulse as seen in Fig. 9.2. As mentioned before in 9.1.1, the analog measurement can only be done for 1 pixel at a time while the digital counting can be done for the complete matrix simultaneously.
Because this measurement is by nature a counting experiment the statistical error on each measured point is given by $\sqrt{counts}$.
Given an ideal pixel, the pulse response for a fixed signal would always be the same. A threshold scan of such a pixel would yield a step function with the step where $|threshold - baseline| = pulseheight$. In reality there is noise caused by digital cross-talk or thermal excitation of electrons in the substrate. The noise induces a variation even for pulses of the same signal which causes the step function to be smeared out into an S-shaped curve. This S-curve can be described with a Gaussian error function which describes the cumulative distribution of a normal distribution.

$$f(x) = \frac{1}{2}(1 + erf(\frac{x-\mu}{\sqrt{2}\sigma})) \tag{9.1}$$

With the parametrization chosen in Eq. 9.1 the noise and the signal height can be obtained. The mean μ of the error function corresponds to the signal height and the width σ to the noise.
When doing this measurement digitally, the number of hits is limited by the number of frames which where evaluated. This can be interpreted as Bernoulli experiment treating each readout cycle as one binary experiment. For a large number of frames the measured value should be close tho the expectation value so that $k \approx \mu = np$ for a binomial distribution, with $p = k/n$ as the probability. With the standard deviation of a binomial distribution one gets Eq. 9.2 for the error of one measurement point.

$$\sigma = \sqrt{np(1-p)} = \sqrt{k(1-k/n)} \tag{9.2}$$

With the so obtained pulse height μ and the noise σ one can calculate the signal-to-noise-ratio (SNR) (Eq. 9.3) with b being the baseline voltage. The SNR quantifies the separation of signal and noise of a detector. It also allows for higher thresholds to suppress the noise while ensuring that the signal surpasses the threshold.

$$SNR = \frac{|\mu - b|}{\sigma} \tag{9.3}$$

This measurement can also be conducted in the absence of a signal to measure the noise level. In that case the μ corresponds to the level at which 50% of the hits are triggered by noise.
A downside of this measurement is that the setting of the DACs, both on PCB and chip side, is imperfect so that sometimes values are left unset or are set wrong. This means that some points of the measurement deviate a lot from their neighboring points and the functional shape or are just 0 and have to be left out. This problem hasn't been examined in a systematic from but has to be addressed in the future.

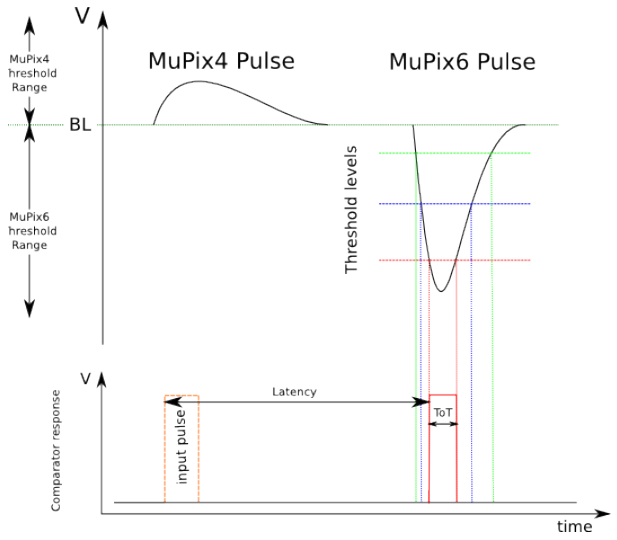

Figure 9.2: Schematic method to reconstruct the pulseshape from [16]

10 Chip Characterization

In this section various measurements and results are shown. Both the MuPix4 and MuPix6 have been studied both to measure their properties and to compare their architecture. The newest prototype, the MuPix7, has been only checked for consistency with the MuPix6 as the only known differences are in the HV distribution and additional digital features.
The MuPix4 chips used for the measurements where 50µm thin while the MuPix6 chips where 250µm thick. No effects of the thickness have been found in [16].
The measurements have been conducted at −60V HV unless stated otherwise. For the MuPix4 only one set of DAC values has been studied while two different settings have been used for the MuPix6. For pixels with only one amplification stage, the DAC values for the MuPix4 where used. The used DAC settings can be found in 12.1. The "high power" settings yield the best shaping while the "low power" settings consume a lot less power. The high power settings have been used unless stated otherwise.

10.1 MuPix4

Although the MuPix4 has been characterized in [23] and [22] some measurements have been done to check for consistency and to allow for comparisons between MuPix4 and MuPix6.

10.1.1 ToT of a Fe55 Signal

Fig. 10.1(a) shows the characteristic ToT spectrum of the iron source measured with the MuPix4. In the center is a gaussian peak from the photo electron. The origin of the tail to shorter ToTs is currently unknown but it has to be a physics process causing these shorter ToTs as this structure is not present in the histogram of an injection pulse (Fig. 10.1(b)). One reason might be the fact that the substrate is not fully depleted and so the fraction of the free electrons, which were created in the depletion zone, drift to the electrode or that the photon was absorbed in a region with a weaker field, which causes a shorter pulse. Another explanation might be that the γ scatters off an electron and the scattered photon has not enough energy for the photoelectric effect left. For photons with a low scattering angle the energy could be enough for a damped ionization which would together with the scattered electron cause less electron-hole-pairs to be created.

However, the photon interaction cross section in silicon seen in Fig. 10.2 for scattering at 5.9keV photon energy is only $3.68\frac{\text{barn}}{\text{atom}}$ while the cross section for photoelectric absorption is 3 magnitudes larger with $7.13\times10^{3}\frac{\text{barn}}{\text{atom}}$, which means that the contribution ofscattering is only a per mill effect.

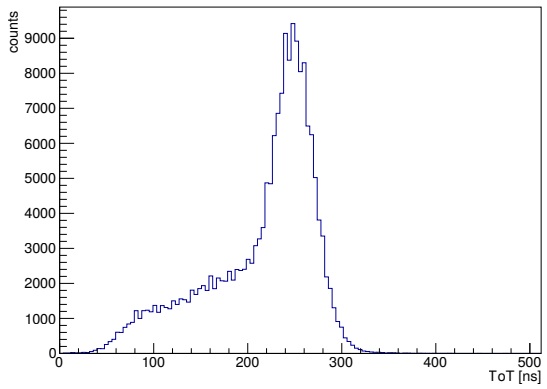

(a) ToT histogram of a MuPix4 pixel with the iron source

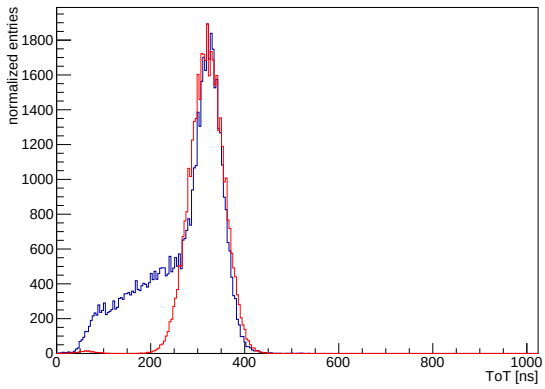

(b) ToT histogram of a MuPix4 pixel with the iron source (blue) and the injection (red).

Figure 10.1: ToT histograms of a MuPix4 pixel

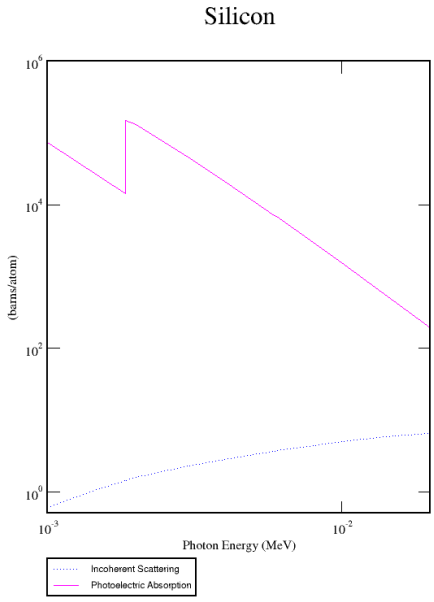

Figure 10.2: Photon interaction cross section with silicon from [40]

10.1.2 Reproduction of previous Measurements

A concern considering MuPix measurements was that some results were difficult or impossible to reproduce. In Fig. 10.3 the ToT was measured 5 times under the same conditions. The other histograms are barely visible under the last drawn histogram which indicates that analog measurements are in principle reproducible.
Previous measurements where done in the climate chamber (section 8.6). To check it the chamber had an additional effect by acting as a Faraday cage, ToT histograms of the same pixel and settings were recorded. The iron source was used as signal. Fig. 10.3 shows that no significant difference can be seen. The chamber was not used for the majority of the measurements in this thesis.
An issue concerning the reproducing of measurements is that the DAC settings are lost sometimes. This can be seen as a drop in consumed current on the power supply for the low voltage input. This issue is known but hasn't been studied in detail so it's unclear whether chip side or PCB side DACs are lost. The power consumption becomes normal again if the DACs are reset. Another issue is that over long scans over many pixels the hitbus isn't enabled properly sometimes. This effect can be reduced by disabling the hitbus before enabling it for another pixel.

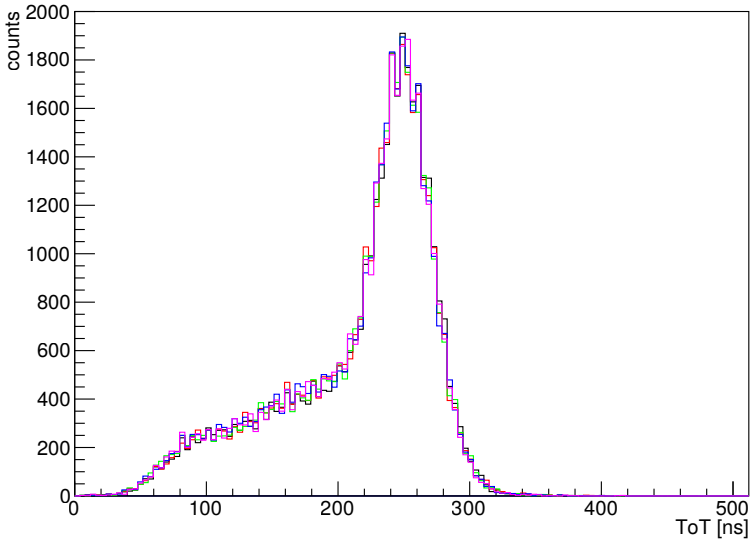

Figure 10.3: 5 ToT histograms of the same pixel with the Fe55 source and the same settings and integration time. The histograms are not normalized.

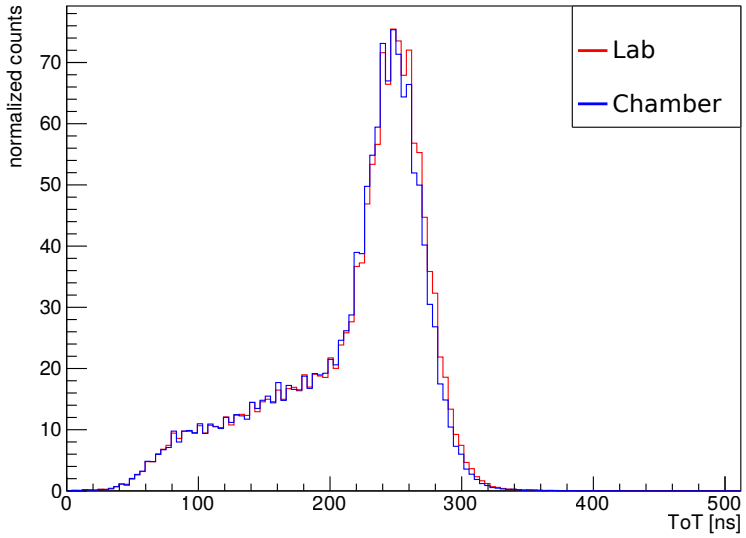

Figure 10.4: ToT histogram of the Fe55 source with (blue) and without (red) the climate chamber. The histograms have been normalized to match each others integral

10.1.3 HV Dependence

For the MuPix6 the HV dependence in the ToT measurements is described in [16]. The MuPix4 on the other hand was never extensively tested for a HV dependence. Only differences between high voltages from 60 to 90V have been observed [22].
In Fig. 10.5 the HV dependence of the signal of the Fe55 source is shown. The histograms in Fig. 10.5 were normalized to each other. The growth of the depletion zone for higher HV which yields a square root like behavior explains the increase in detected Fe55 γ's detected in Fig. 10.6(a). For large HV the ToT starts increases exponentially as the diode is nearing the breakthrough voltage which can be seen in 10.6(b). With a higher HV, charges can also be collected faster which induces a larger pulse in the CSA which is shaped into a longer pulse causing longer ToTs. Fig. 10.5 shows that for large HV a tail to longer ToTs starts to form. This is caused by the high electric field which causes secondary electrons to create tertiary electron-hole-pairs for some cases.
The same measurement was performed for a pixel on another MuPix4 chip but with the same integration time for each point and for more voltages in Fig. 10.6. For this pixel the dependence is smaller but the form is the same. A reason might be chip to chip or pixel to pixel variances from the production process.

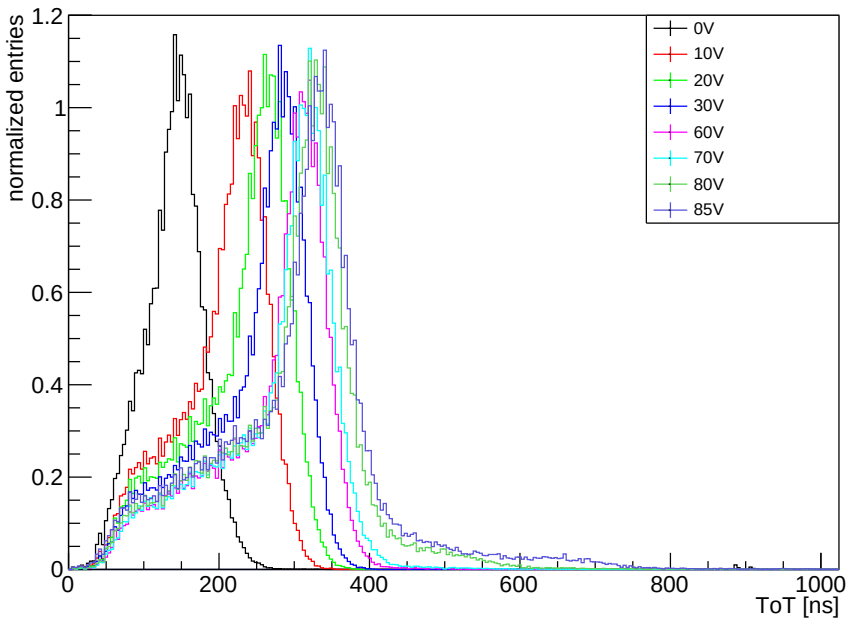

Figure 10.5: HV measurements of a single MuPix4 pixel and the same settings with the iron source. Histograms are normalized.

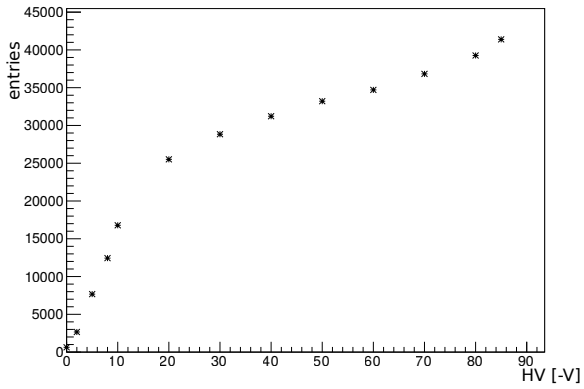

(a) Number of detected pulses

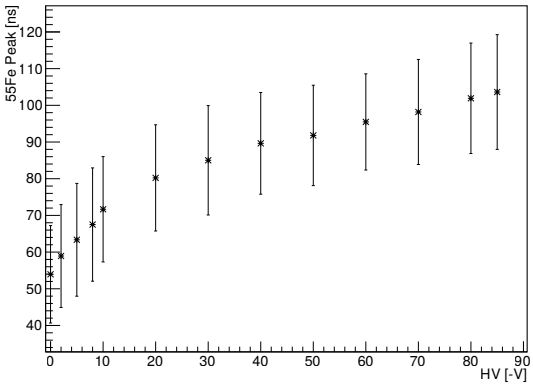

(b) ToT peak vs HV

Figure 10.6: HV measurements of a single MuPix4 pixel and the same settings with the iron source on a different MuPix4 chip than Fig. 10.5.

10.1.4 Spatial Dependence

To look for dependencies in the ToT distribution depending on the position of the pixel on the chip, multiple pixels have to be scanned. As a scan over all pixels would take too long only a sample of pixels was chosen to see if there are any systematic effects in the chip-wide distribution. Longer ToTs for pixel with a higher row position were expected as their signal lines to the digital part are longer than the lines of pixels with lower row values. In Fig. 10.7 a ToT scan over a MuPix4 chip is shown. The pixel map shows that most of the pixels have a rather uniform ToT compared to a few pixels which deviate a lot from the mean. These deviating pixels are randomly located in the pixel matrix
This measurement was conducted with a subset of pixels on one chip so there may be other chips which exhibit systematic differences between pixels.

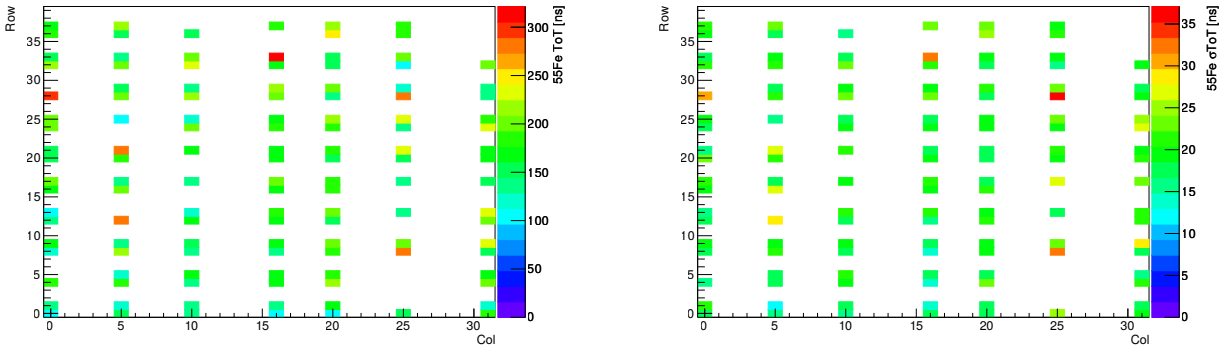

(a) ToT peak map of the chip

(b) ToT width map

Figure 10.7: Mean and width of the ToT of the iron signal of pixels on the same columns and use the same injection testpulse for a MuPix4. Omitted pixels were either not measured or the data was not conclusive.

10.2 MuPix6 Comparison

As previously mentioned, a detailed characterization of the MuPix6 can be found in [16]. In this section comparisons between the MuPix6 and MuPix4 are described. The results of these comparisons are necessary to decide for the analog structure of future MuPix prototypes.

10.2.1 ToT of a Fe55 signal

Fig. 10.8 shows the ToT distribution of the iron source measured with a MuPix6 pixel. Like for the Mupix4 in section 10.1.1 a Gaussian peak with a tail to short ToTs is present. Additionally a peak at the lower end of the tail and an even greater peak for very short ToTs are visible.
To test if this was a physical signal or a property of the electronics the measurement was repeated for different threshold settings for the same integration time. If the additional peaks were a very weak physics signal, they would shrink and vanish for higher thresholds. The result is shown in Fig 10.9. Instead of decreasing, both peaks grow in size as the Fe peak moves closer zero. As both the tail-end and the Fe peak start to merge, the tail-end and the very short ToT peak lose intensity very rapidly. This indicates that this effect is not a physics feature but a feature of the analog electronics as it depends on the intensity of the iron peak.

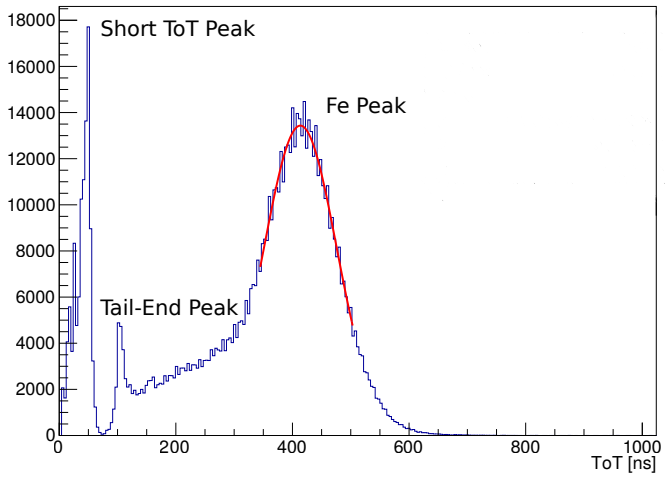

Figure 10.8: ToT histogram of the iron source with a MuPix6 pixel

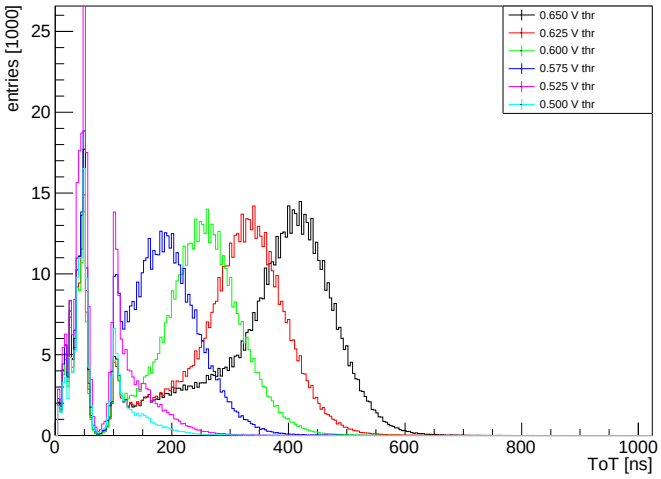

Figure 10.9: ToT histograms of the iron source with a MuPix6 pixel for different thresholds

10.2.2 Comparator Oscillation

The oscillation of the comparator of the MuPix6 described in [16] make an ideal candidate for the new ToT structures seen in section 10.2.1. An oscillation in the analog part of the pixel could modulate the main pulse such that the peak is smeared out and that on the edges short pulses could emerge. Fig. 10.10 shows a qualitative sketch how such a modulation through the oscillation impacts the comparator. With a threshold like in the drawing the effective pulse is shorter and a short after pulse would be seen. For higher thresholds the pulse could be affected even more depending on the phase of the oscillation.
A look at the hitbus output with the oscilloscope reveals a periodic signal for low thresholds even if the amplification stages are off as seen Fig. 10.11. For small signals, e.g.low injection voltages, the oscillation could modulate the pulse sometimes into one short or two short pulses. If only one short pulse is generated it can be resolved by the FPGA, but two pulses can't be resolved so clearly. This allows the short peak to be identified with one short pulse and the tail-end peak with two pulses that the FPGA merges together. The merging of the pulses could also be caused by the LVDS transmission because it prolongs the pulses. The assumption that pulses merge is strengthened by the fact that the tail-end peak equals roughly double the ToT of the short ToT peak. Because double pulses are rarer in comparison to single pulses the tail-end peak has less counts than the other one as seen in Fig. 10.9.

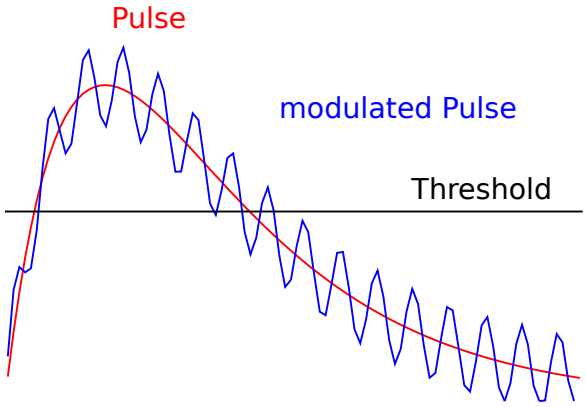

Figure 10.10: Sketch of the pulse modulation which illustrates a scenario with short after pulse

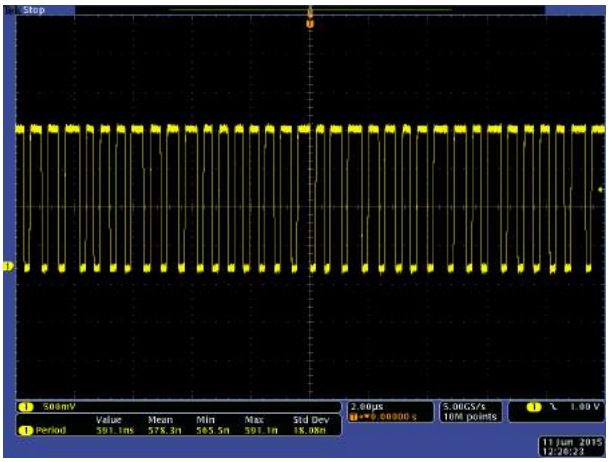

Figure 10.11: Comparator output at low thresholds with the amplification stages switched off

These additional peaks can also be seen when measuring with an injection like in Fig. 10.12. The additional peaks are heavily suppressed compared to the injection peak. Taking the thresholdscan in Fig. 10.9 also into account, this is a strong indication that the effect is depended on small signals but can also occur on larger signals. This could be due to the longer falling edge compared to the ToT so the chance for the oscillation to be at the right time to push the falling edge over the threshold again for a short time. Looking at the hitbus output with the oscilloscope (Fig. 10.16) reveals short afterpulses after an injection pulse.

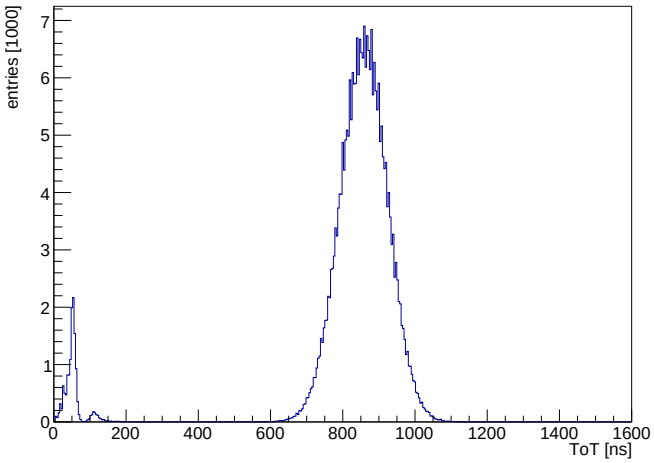

Figure 10.12: ToT histogram of a MuPix6 pixel with an injection as source

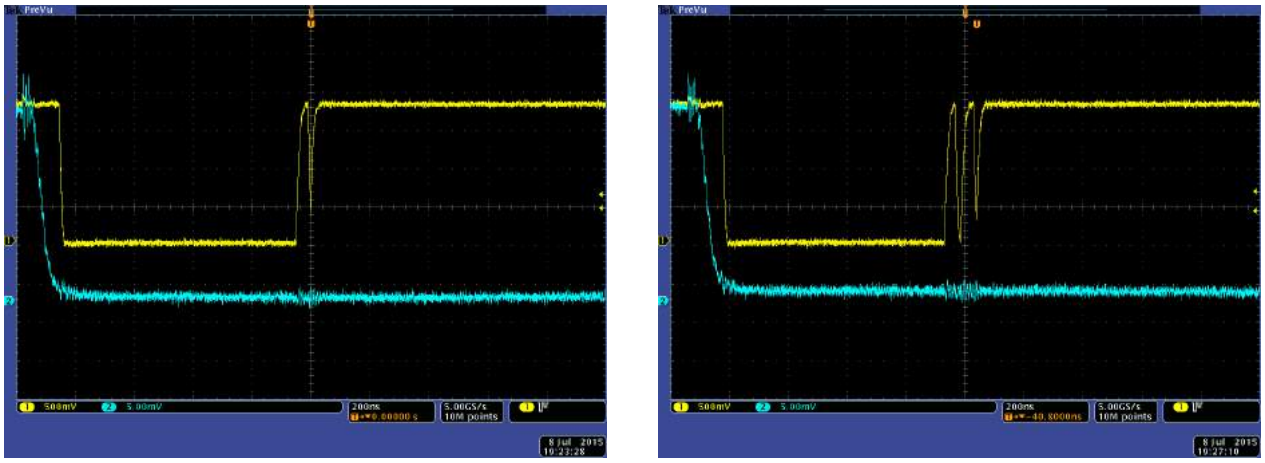

(a) Comparator pulse with one afterpulse (yellow) and the triggering injection (teal)

(b) Comparator pulse with two afterpulses (yellow) and the triggering injection (teal)

Figure 10.13: Oscilloscope image of afterpulses triggered by an injection

To check if this behavior is also present in the MuPix4 design also pixels on a MuPix4 chip where tested with the source follower and the amplification stage turned off. Fig. 10.14 shows that an oscillation can also be found in the MuPix4. It seems that for the MuPix4, pulses get modulated less and the comparator is more robust against oscillations.

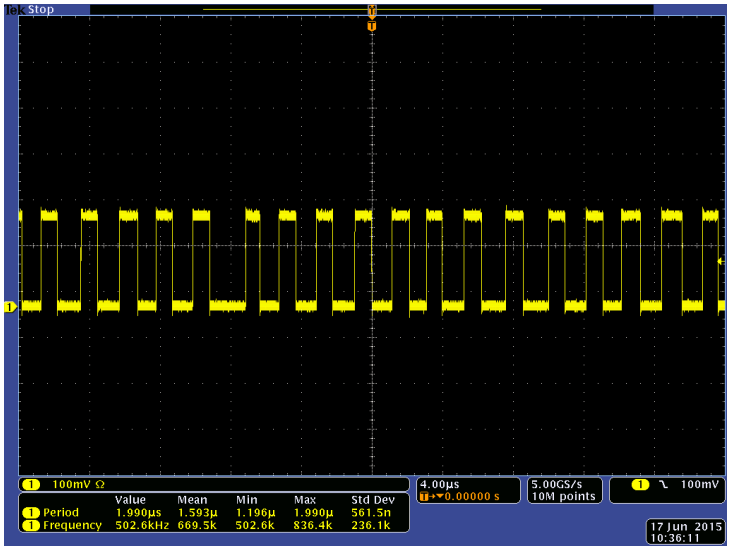

Figure 10.14: Comparator oscillation in a MuPix4 pixel

The oscillation frequency can be controlled with the BlRes DAC. The higher the DAC value the higher the frequency as seen in Fig. 10.15. The same effect was also observed for MuPix6 pixels with only one amplification stage which were used with BlRes = 0x3C. Fig. 10.16(a) shows that the two additional peaks are still present. This indicates that the problem is on the comparator side. To check if a modulation could be seen with a MuPix4 if the BlRes DAC was lowered, the ToT histograms for low BLRes values were recorded. As seen in Fig. 10.16(b), no additional peaks emerge.
To measure the amplitude of the oscillation, the threshold was increased until the oscillations were visible. The threshold was then increased even more to find the point where no pattern could be seen on the oscilloscope. At this point the voltage difference between baseline and threshold was measured directly at the special testpoints on the PCB to circumvent any offset between the the GUI threshold and the threshold on the PCB. This gives an upper limit on the amplitude.
Amplitudes vary from pixel to pixel and are of the order of $\mathcal{O}(10-20\text{mV})$. A correlation between higher amplitudes and so called "hot" pixel, pixel which are noisier and have a higher threshold for noise, has not been observed.

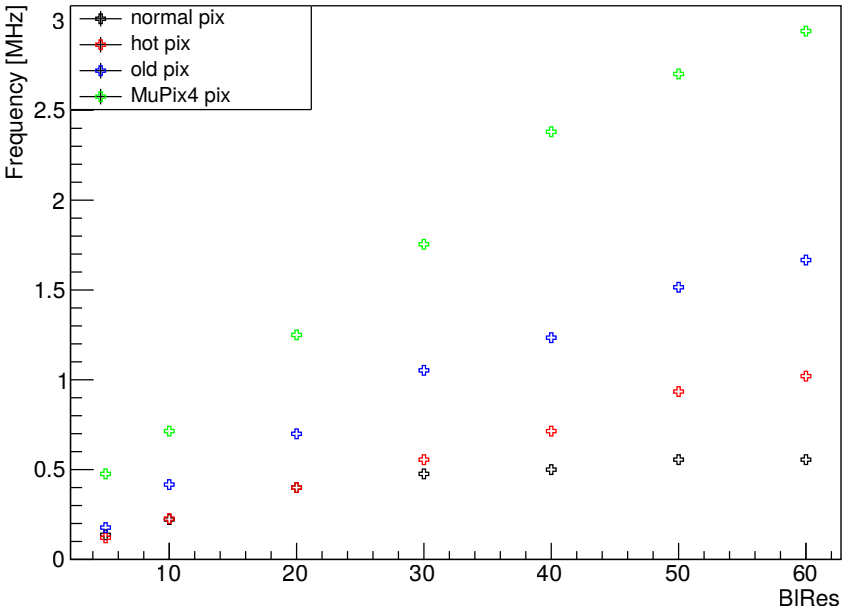

Figure 10.15: Plot of the BlRes dependence of the oscillation. The period was measured and the frequency calculated from the period. The values are not representative as the noise introduces variations in the period for multiple measurements and only one pixel was measured for each type. "old pix" refers to an one staged pixel on a MuPix6 chip.

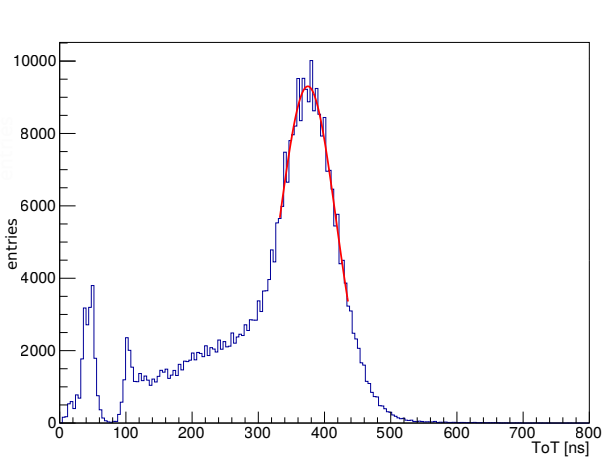

(a) ToT histogram of a single staged MuPix6 pixel with the iron source

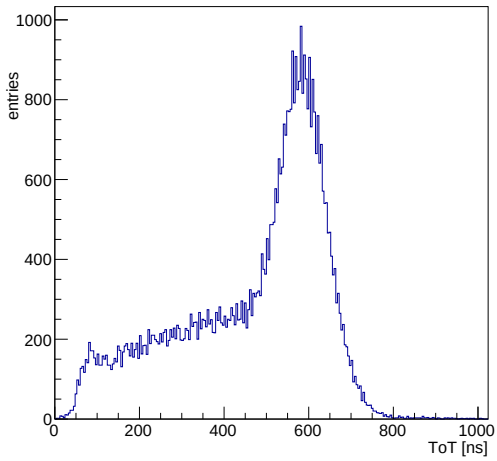

(b) ToT histogram of MuPix4 pixel with the iron source with BlRes = 0x5)

Figure 10.16: ToT histograms of a single staged MuPix6 pixel and a MuPix4 pixel with low BlRes. The iron source was used as signal.

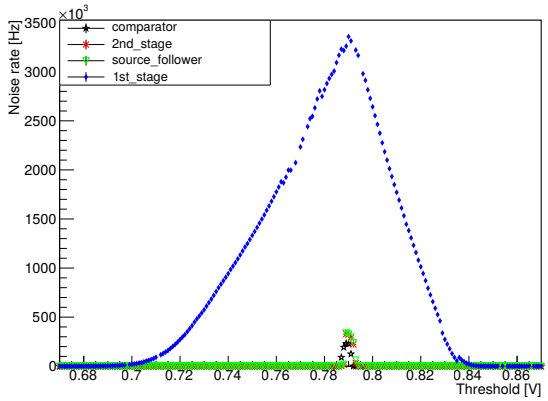

(a) Noise rate depending on stages switched on. The names in the legend refer to the stage that was last switched on. This means that the mentioned stage and every stage afterwards is turned on while every stage before is turned off

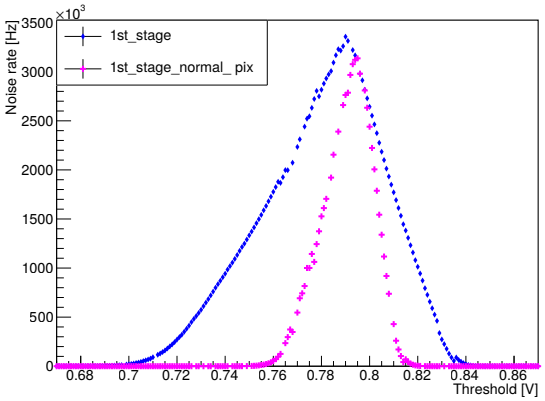

(b) Noise rate with full amplification for a hot pixel (blue) and a normal pixel (magenta)

Figure 10.17: Analog noise rate measurement for a hot pixel and comparison with a normal pixel on a MuPix6

10.2.3 Noise

The oscillation in the analog part of the pixel described in section 10.2.2 could cause ringing in the pixels, leading to more noise hits. To measure this analog threshold scans were performed to count the number of pulses. The first scan had only the comparator switched on and the rest switched off. For the following scan more stages where added: first the second amplification stage, second the source follower and last the first amplification stage. Fig. 10.17(a) shows the result of this measurement for a hot pixel. It shows that the comparator noise makes up only a small fraction in a small threshold width. The noise from switching the first amplification on dominates it by orders of magnitude. This leads to the conclusion that the noise originates in the first amplification stage or in the parts before, namely the diode and the detection electrode. A similar behavior was also observed in [16].
Fig. 10.17(b) shows the comparison of the noise level with the full amplification scheme for a normal and a hot pixel. It shows a similar rate at the peak and and similar shape but with a much smaller width. The rate is limited by the shaping because the compartor can't resolve all the noise pulses at some point which causes the pulse rate to decrease. The reason might be production errors in the doping or the electrode which cause more noise or an increased sensitivity to noise.

10.2.4 Spatial Dependence

Like for the MuPix4 in section 10.1.4, the ToT of multiple pixels in the same column on a MuPix6 have been measured in Fig. 10.18. The average ToT is lower because the noise level on the MuPix6 chip is higher than on the MuPix4 so the threshold has to be chosen higher. On the tested MuPix6 chip no structures were visible.

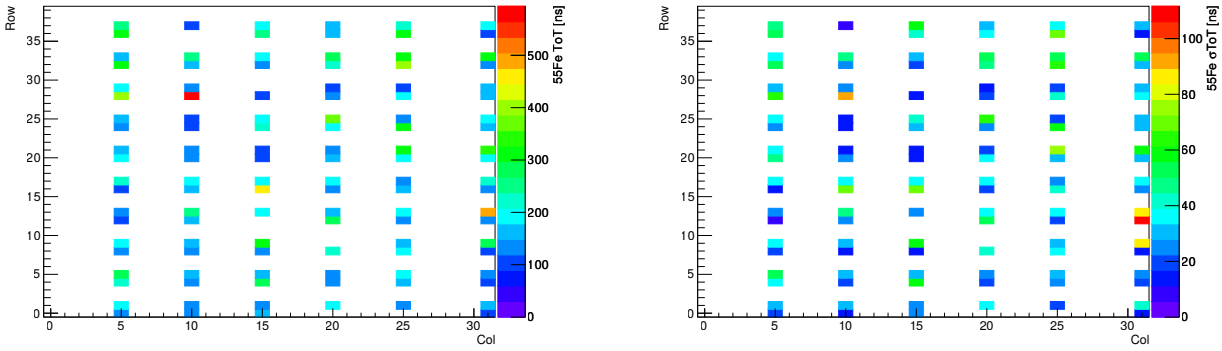

(a) ToT peak map of the chip

(b) ToT peak width map

Figure 10.18: ToT and width of an iron source of pixels on the same columns which use the same testpulse injection of a MuPix6. Omitted pixels were either not measured or the data was not conclusive.

10.2.5 Pulseshape

When the first MuPix7 chip was in a state to be read out, it's functionality was tested. Because it's analog structure should be identical to the MuPix6 pulseshape measurements described in section 9.3.2 were done to compare the pulse response of the chips. To reconstruct the pulseshape, the delay to an injection pulse and the duration of the comparator pulse were measured multiple times and averaged. This was repeated for multiple thresholds to reconstruct the pulseshapes seen in Fig. 10.19. The general shape is the same and small differences are expected due to inhomogeneities in the production. The pulseheight varies from pixel to pixel as the sensor electrodes are not equally large due to the fabrication uncertainties [38].

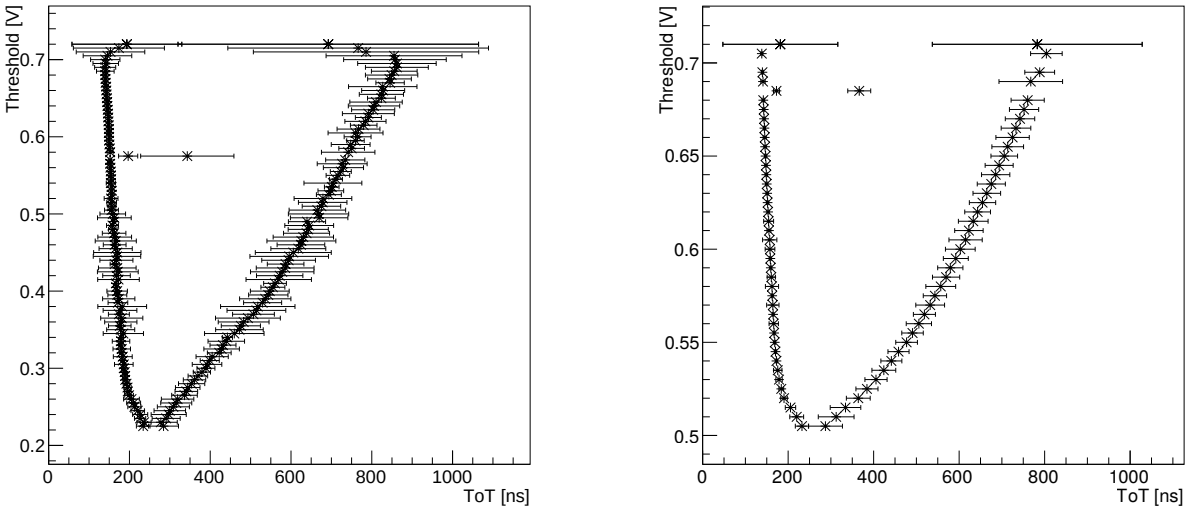

(a) Pulseshape of a MuPix6 pixel

(b) Pulseshape of a MuPix7 pixel

Figure 10.19: Pulseshape of a MuPix6 and a MuPix7 pixel with 1.5V injection at −70V HV. The MuPix6 and MuPix7 pulse is negative and the baseline is at 0.8V so the pulse points downwards. The top and bottom part of the pulse where cut off because the comparator doesn't work properly for small ToTs as seen in 10.2.2 and for thresholds very close to the baseline because there is too much noise.

10.2.6 X-Ray Measurements

The X-ray setup described in section 8.3 was used to measure the minimal detection energy of the MuPix6. Because only the hitbus cable could fit through the cable canal after all other cables which are necessary to operate the MuPix were pulled through, only analog measurements were performed.
The ToT was measured at different X-ray energies. At first, the setup was used to get very monochromatic X-ray photons via Bragg-reflection off the crystal lattice. This approach was abandoned as it turned out that not enough intensity was left after reflection so that integration times of 2h or longer were necessary to acquire reasonable statistics. The additional information concerning the X-ray experiment provided by PHYWE [41] in Fig. 10.20 shows that only 4 spectral lines of the tungsten anode have very high intensity. The other lines are probably not resolvable by the MuPix in reasonable time.
Instead another approach was pursued. The voltage between the cathode and anode of the X-ray tube sets the a limit to the energy the photon can have. This means that the longest ToT should correspond to the maximum energy. The maximum energy is then the voltage times the electron charge (Eq.10.1) so that a voltage of 15kV equates 15keV.

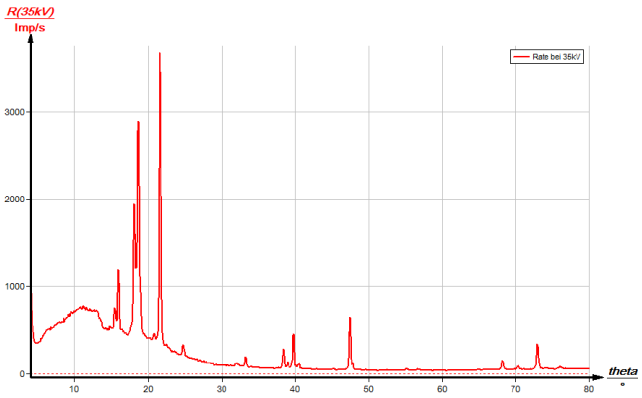

Figure 10.20: X-ray spectrum of the tungsten anode measured with the LiF crystal depending on the angle [41]

At less then 7kV electrode voltage the rate became too low to make conclusive measurements, so the measurement points only go as low as 7keV. For the future, other sources and setups will be evaluated to measure energy depositions closer to the experimental signal.

$$E_{\gamma,max} = E_{e,max} = e \cdot U \tag{10.1}$$

An example of a ToT histogram is shown in Fig. 10.21. To approximate the maximum ToT, a straight line was fitted to the falling edge to longer ToTs. The extrapolated zero crossing is then taken as the maximum ToT. The result can be found in Fig. 10.22(a). To fit the voltage dependence it was assumed that the change in energy was affecting the falling edge of the pulse much more than the rising edge of the pulse so that the rising edge could be ignored. This corresponds to a simplified pulseshape model where the ToT is described by an exponential decay which in turn causes a logarithmic behavior of the ToT given the energy of the photon. For high energies this seems to be a reasonable assumption. The fits all intersect the X-axis at energies below 2keV which is half of the expected energy deposition of the low momentum electrons in the experiment.
To check if this was also the case for the MuPix7, this measurement was repeated for a MuPix7 chip in Fig. 10.22(b). No significant differences could be observed.

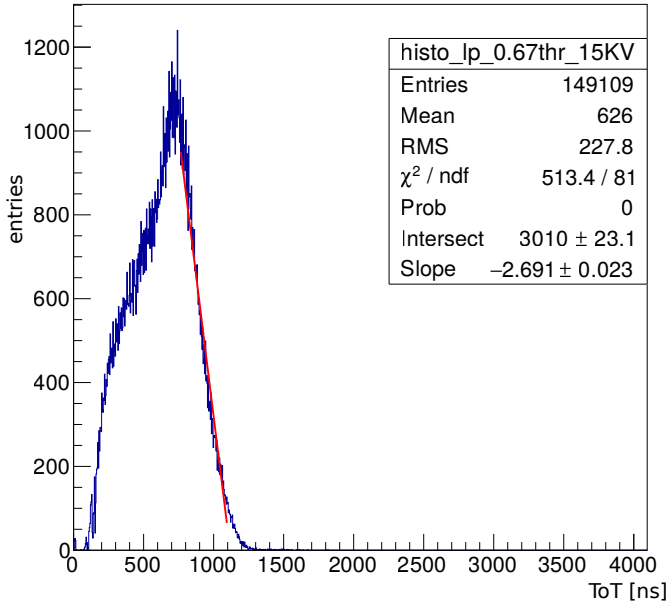

Figure 10.21: ToT of a pixel with low power settings and 0.67V threshold. The voltage between the electrodes of the X-ray tube was 15kV

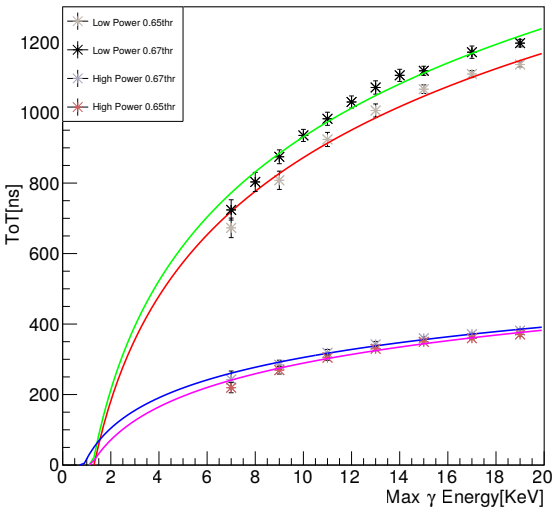

(a) MuPix6

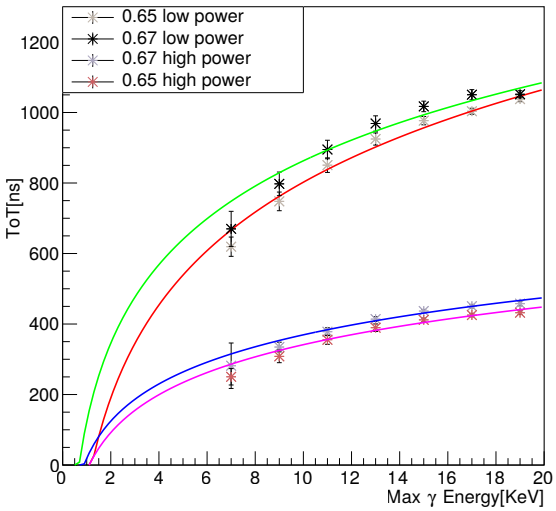

(b) MuPix7. The numbers in the legend denote the used threshold

Figure 10.22: Extrapolated ToT vs the maximum energy of the X-ray at different thresholds and with different settings and logarithmic fits.

10.3 Threshold Tuning for individual Pixels

Tuning describes the procedure of adjusting the threshold of each pixel individually with the help of the TDACs. This is done to correct deviations of individual pixels which can occur in the fabrication process. The maximum shift is set by the VPDAC value which is subdivided by a 4 bit DAC which can be set for each pixel individually.
The challenge of the tuning procedure is to set the dynamic range with VPDAC high enough to tune all the pixel enough but not too high because the tune system consumes a lot of power. In an optimum tuned state on would expect a gaussian TDAC distribution with the mean of 7 which has entries in all bins. The linearity of VPDAC and the TDACs was measured in [16].
To find the best method, however, is depending on the goal. To achieve a uniform response for all pixels tuning with a signal is probably the best option. This has the downside that a generation of such a reference signal is very difficult as described in section 10.4. The spatial measurements in section 10.1.4 and 10.2.4 have shown large deviations concerning the response of the pixels to the same signal.
Another way is tuning with noise. For this method the threshold is tuned such that all pixels have less noise rate than a predefined limit. This in turn means that some pixel might be less sensitive to signals than others, assuming that noise rate and amplification aren't correlated.

10.3.1 Noise Tuning

Because noise rates are an important limitation for the operation of the Mu3e experiment noise tuning was studied in detail. The big advantage is that it can be done in situ and without any calibration or additional signal. In the following a tune method and it's results are presented.
The steps are as following:

- Choose a noise rate limit
- Find a threshold for which all pixels are producing noise hits
- Set all TDACs to the max value, 15, and increase VPDAC until no pixel surpasses the noise limit
- Set all TDACs back to 0
- Measure the noise rate over a set amount of time and increase the TDAC for each pixel which has a higher noise rate than the limit
- Repeat the previous step until one reaches the maximum TDAC value or until all pixels have a noise rate below the limit, which ever comes first

The TDAC iteration has been fully automatized but the method to find the right VPDAC value doesn't work automatically. For the tune results presented in this thesis the VPDAC value was set manually. To compare the tuned with the untuned state a measurement was implemented which measures the noise level in each pixel for different thresholds. The results vary because noise is a statistical effect but the variations are fairly limited.
Fig. 10.23 shows the distribution and the pixel matrix of the 0.1Hz noise rate threshold of an untuned MuPix6 chip. For each pixel the noise rate was measured for each threshold and the threshold at which the pixel has more noise than the chosen maximum noise rate was recorded. For the following results 0.1Hz noise rate was chosen and each for threshold the rate was measured for 30s. The "white" pixel in the center is the pixels for which the hitbus was enabled which may have caused this pixel to be not read out correctly. The threshold was set to 0.74V because all pixel had noise hits at this threshold as seen in Fig 10.23(a).
After the VPDAC value was found manually, the pixels where tuned as previously described. The maximum noise rate per pixel was set to 0.1Hz. For each TDAC value, the noise rate was measured 100s. The pixel matrix with the TDAC values in Fig. 10.24(b) shows a strong correlation with the noise level matrix in Fig. 10.23(b). The distribution of TDAC values in Fig. 10.24(a) is roughly Gaussian like expected.

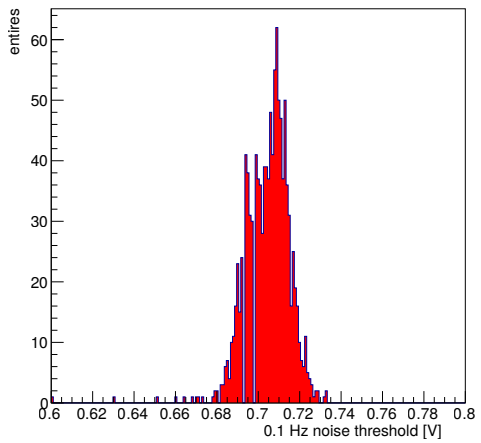

(a) 0.1Hz noise rate threshold distribution

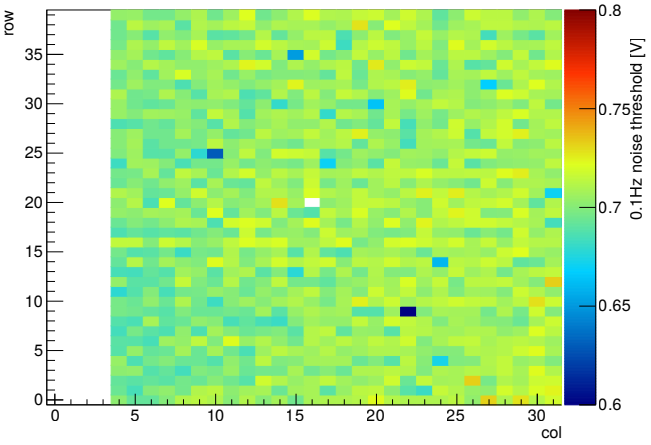

(b) 0.1Hz noise rate threshold pixel matrix

Figure 10.23: 0.1Hz noise level threshold of a MuPix6

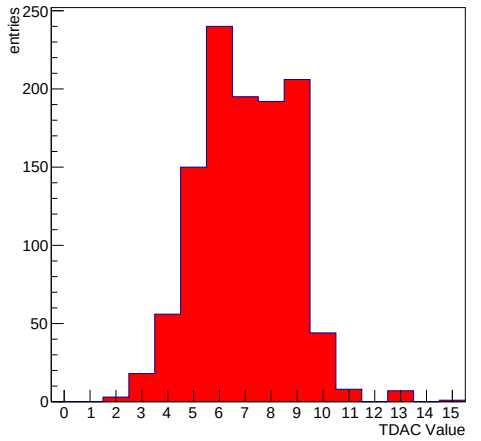

(a) TDAC distribution

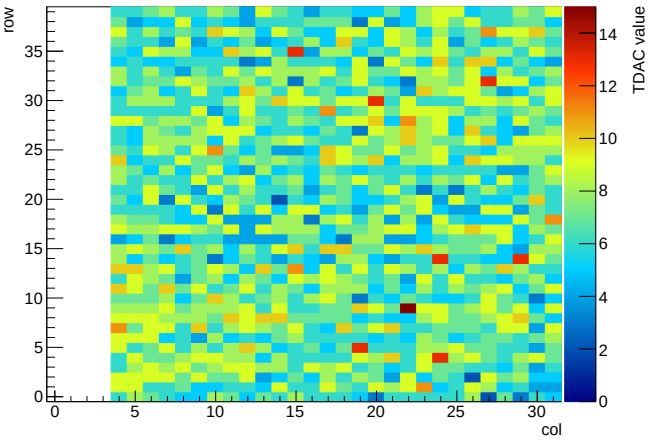

(b) TDAC pixel matrix

Figure 10.24: TDAC values after a tune to 0.1Hz noise rate

The 0.1Hz noise rate threshold was measured again after tuning and is displayed in Fig. 10.25. The width of the distribution in Fig. 10.25(a) has decreased significantly in comparison to the untuned state in Fig. 10.23(a). The pixel matrix for the 0.1Hz noise rate threshold looks also more uniform than before in Fig. 10.23(b). The width was of the 0.1Hz noise rate threshold distribution was also significantly smaller after tuning. Before tuning the full-width-half-maximum (FWHM) of the distribution was $\approx$ 35mV in Fig. 10.23(a) and after tuning $\approx$ 10mV in Fig. 10.25(a).

In Fig. 10.26 the 0.1Hz noise rate threshold before and after tuning against their respective TDAC values is shown. Fig. 10.26(a) shows a clear anti-correlation between TDAC values and the 0.1Hz noise rate threshold before tuning. After the tuning, the 0.1Hz noise rate threshold is uncorrelated as seen in Fig. 10.26(b).

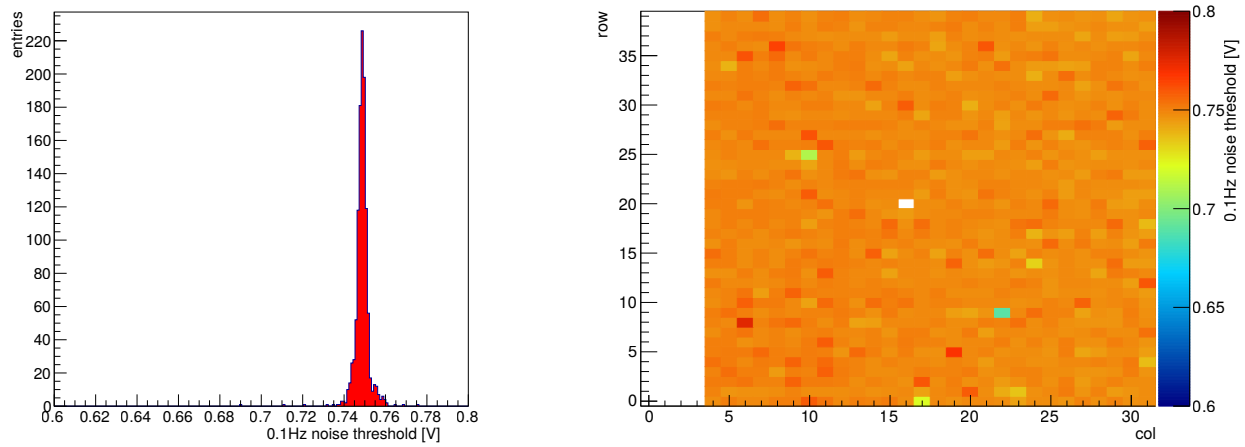

(a) 0.1Hz noise threshold distribution after tuning

(b) 0.1Hz noise threshold pixel matrix after tuning

Figure 10.25: 0.1Hz noise rate threshold after tuning

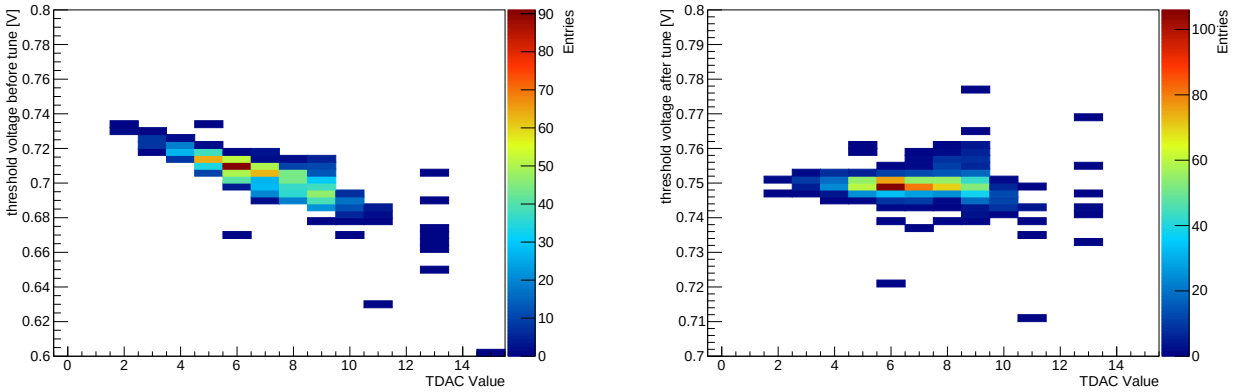

(a) 0.1Hz noise rate threshold before tuning vs TDAC value

(b) 0.1Hz noise rate threshold after tuning vs TDAC value

Figure 10.26: 0.1Hz noise rate threshold vs TDAC value before and after tuning

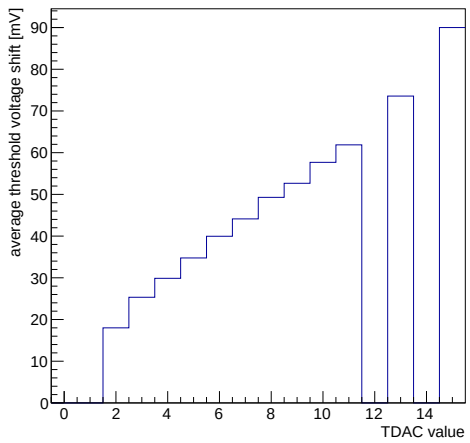

(a) Average 0.1Hz noise rate threshold shift per TDAC value. Empty bins are due to no pixel having the corresponding TDAC value (Fig. 10.24(a))

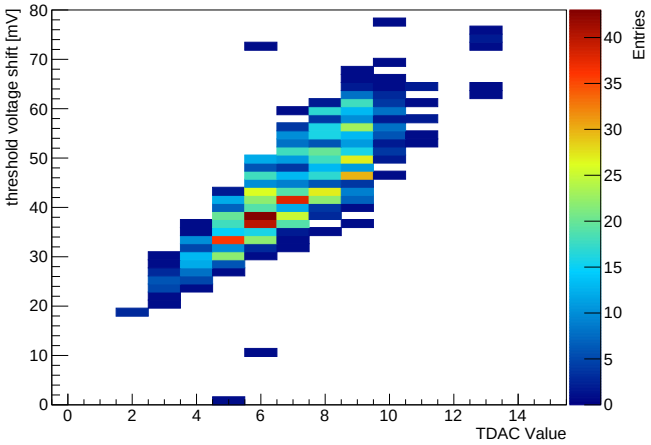

(b) 0.1Hz noise rate threshold shift

Figure 10.27: 0.1Hz noise rate threshold differences between the tuned and untuned state. The TDAC value chosen by the tune procedure for a pixel is anti-correlated to 0.1Hz noise rate threshold that was measured before tuning. After the tuning there is no correlation between TDAC value and 0.1Hz noise rate threshold .

To quantify this improvement the voltage shift between the tuned and untuned noise levels were calculated and plotted in Fig. 10.27. The average noise threshold shift in Fig. 10.27(a) shows a linear behavior. The histogram representation of the shifts of all pixels vs their TDAC value is show in Fig. 10.27(b). A linear dependence can also be seen here but it's smeared out. One reason for this could be the limited statistics. Another explanation could be that the TDACs have slight variation from another so that they may be linear but with a different slope.
Also data runs were taken for the tuned and untuned chip, as well as tuned runs with the iron source at the same threshold that was used for tuning. For the untuned chip in Fig. 10.29, the noise rates are distributed over all frequencies and saturate at 1.5kHz which was the readout cycle rate for the run. This means the pixel had stored a noise hit every time they were read out. After tuning (Fig. 10.28) the noise rate is almost 0 but a few "hotter" pixel remain, so the method isn't perfect or VPDAC was chosen too low. Maybe some TDACs were not written correct or got lost. The measurement the iron source in Fig. 10.3.1 shows that all pixels see can detect the iron source but at different rates as seen in Fig. 10.31. This could be due to statistical limitations or an inhomogeneity of the iron source, but it's more likely that some pixel have such a high threshold that the tail from photons who convert at the edge of the depletion zone as described in section 10.1.1.

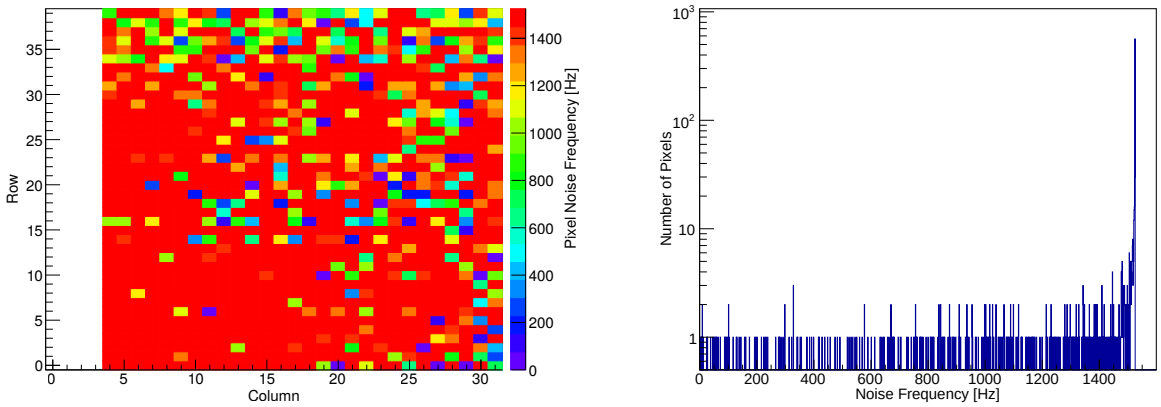

(a) Untuned noise hit map of the chip

(b) Untuned noise hit rate per pixel

Figure 10.28: Noise of an untuned chip

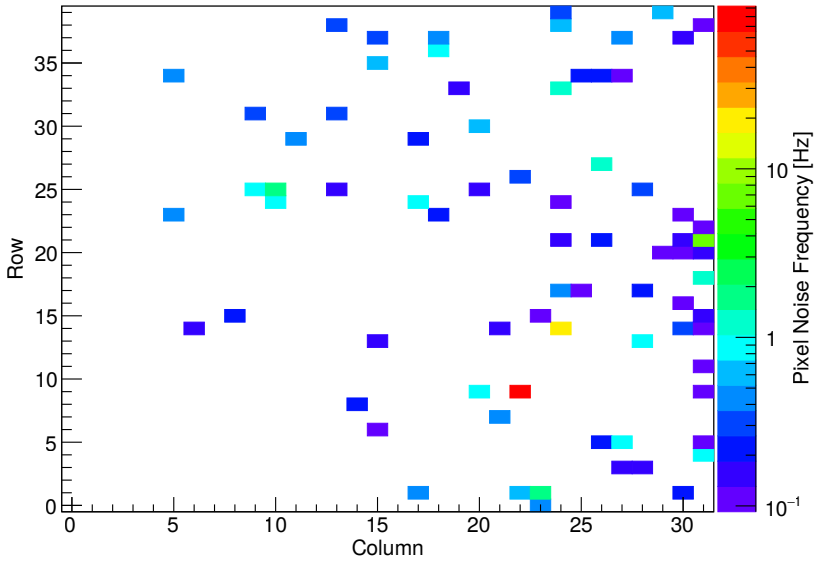

Figure 10.29: Tuned noise hit map of the chip

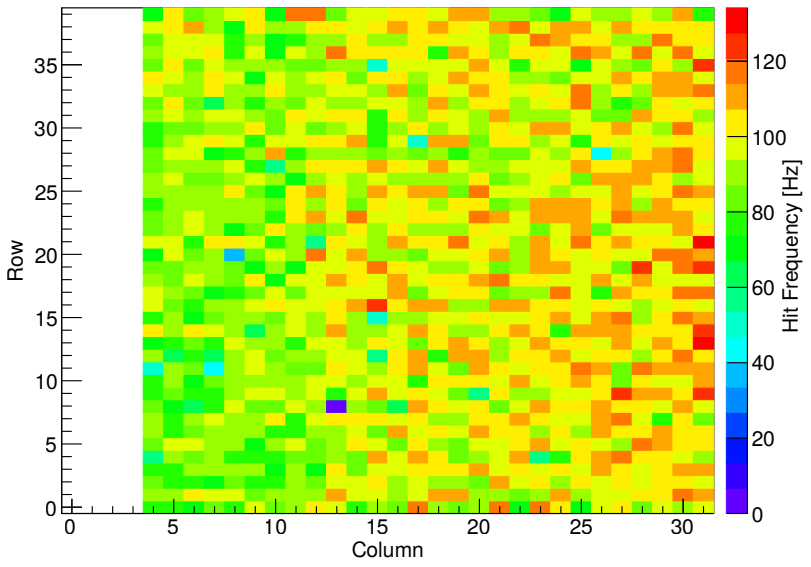

Figure 10.30: Hit map of the tuned chip with the iron source

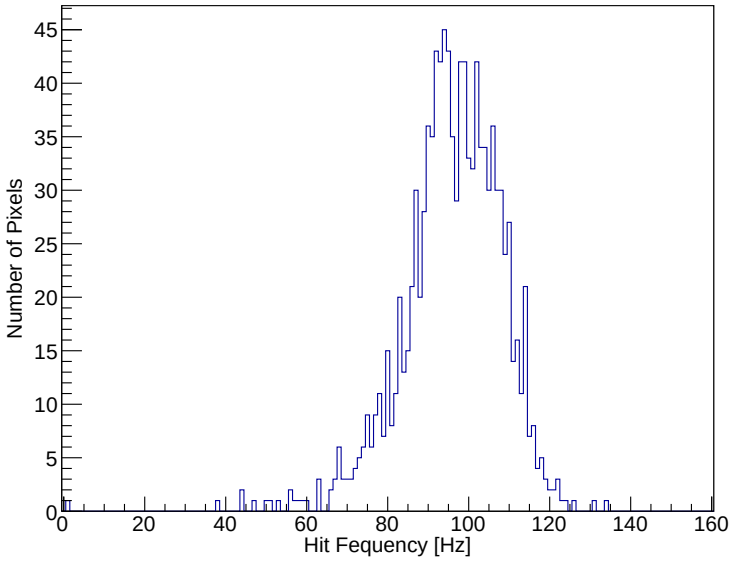

Figure 10.31: Hit rate per pixel of the tuned chip with the iron source

10.4 SNR

As mentioned in section 9.3.2, the SNR characterizes the separation of noise and signal of a detector system. Because BR($\mu \rightarrow eee$) is very small, the efficiency for the electron detection has to be very high. The noise rate on the other hand has to be low in order to not surpass the bandwidth limitations of the detector as well as to reduce the necessary computation power of the online filter farm.
The most common signal for calculating the SNR is the Fe55 source. The photon energy of 5.9keV is one of the lowest for easily available radioactive sources and monoenergetic. It is close to the deposited energy of a low momentum electron in the $\approx$ 10µm thick depletion zone of the MuPix of $\approx$ 4keV as explained in section 5.3.
The downside of the iron source is that the decays are stochastic and the readout can't be triggered to look for the γ as its only interaction is the photoelectric effect that causes the photon to be absorbed. A threshold scan (9.3.2) to fit the S-curve (Eq. 9.1) is very difficult because the rate per pixel is very low so a long integration time would be needed. A workaround is to calibrate the injection to have the same amplitude as the iron source signal. This yields a comparable signal as the iron source and it is timed such that only one injection pulse is generated during one readout cycle. However, the this calibration is only correct for that pixel as other pixels need different injection voltages due to production uncertainties [38]. This makes the measurement of a lower SNR limit difficult because error on the capacity of the pixel and the error on the injection capacity are not correlated.
The original intent of this thesis was to measure the SNR for all pixels at the same time to obtain a chip wide distribution. However, the method to measure the SNR for all pixels without calibrating the injection for each pixel individually is still object of discussions. THe SNR has been measured for single pixels in [22] and [16].
The SNR isn't the figure of merit for the Mu3e experiment because a stable working point with high efficiency with low noise rate are required to operate the detector successfully. This point however can't be found easily in the lab but has to be found in test beam data [42]. Test beam results have the big advantage that the particle tracks can be reconstructed and one can compare the amount of tracks which were reconstructed and the number of those track that have a matching hit in the sensor. Also the energy deposition isn't discrete like the deposition of photons but Landau distributed as it is the case in the experiment.

10.4.1 Pulseheight Measurements

To measure the SNR analog threshold scans were performed. This measurement is not effective for a chip wide SNR measurement because only one pixel can be measured at a time. A digital pulseheight measurement could be performed in shorter time and for the complete pixel matrix at the same time. However there is no a priori insurance that the analog ToT and the digital pulseheight are linked.
To measure the dependency between pulseheight and ToT, both were measured for different injections and than plotted in Fig. 10.32. As seen before in Fig. 10.22, the ToT shows a logarithmic dependence on the collected charge, which is proportional to the injection voltage, while the pulseheight shows a linear behavior.
The S-curves (Eq. 9.1) can be found in Fig. 10.33. When plotting the ToT against the pulseheight this logarithmic behavior can be seen (Fig. 10.34). This is consistent with the approximations in section 7.2.3. The exact functional behavior, however, depends on the shaping parameters. The pulseheight plotted here is corrected by the baseline voltage.
The pulseheight and ToT were also measured for a pixel with one amplification stage on the MuPix6 (Fig. 10.4.1 and a MuPix4 (Fig. 10.4.1) pixel. The functional behavior seems to be the same.

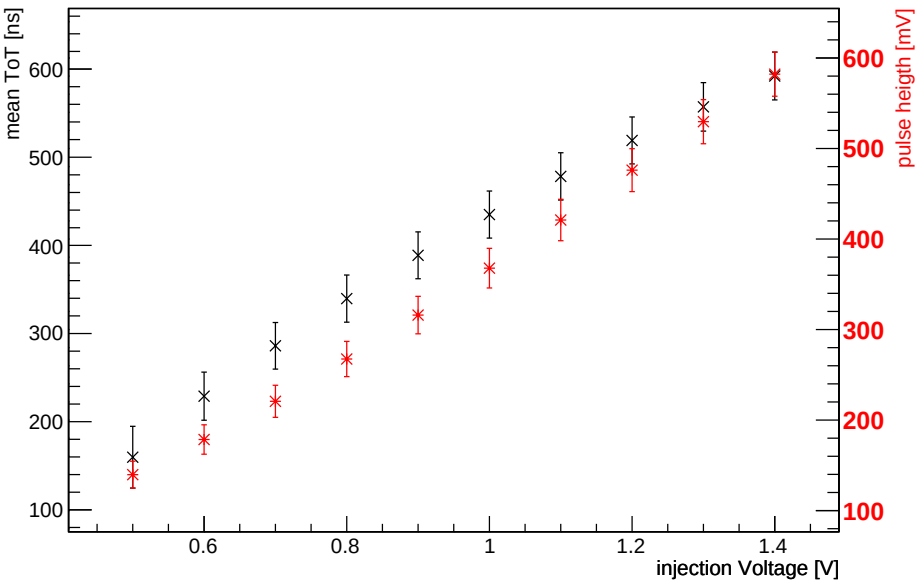

Figure 10.32: ToT and pulseheight for a MuPix6 pixel at various injection voltages

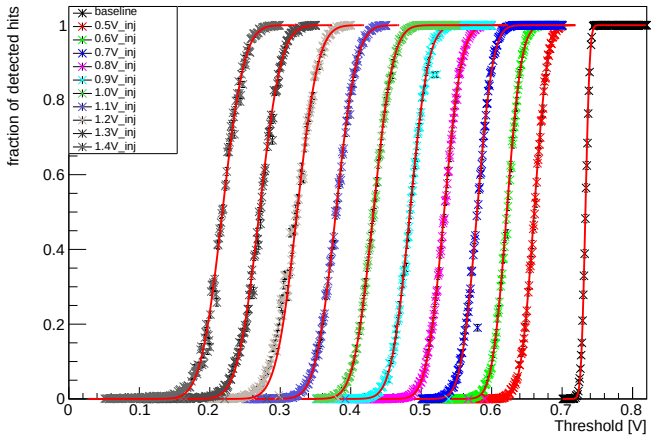

Figure 10.33: S-curves for a MuPix6 pixel for different injection voltages. Baseline denotes here that no injection was used so it records the noise level.

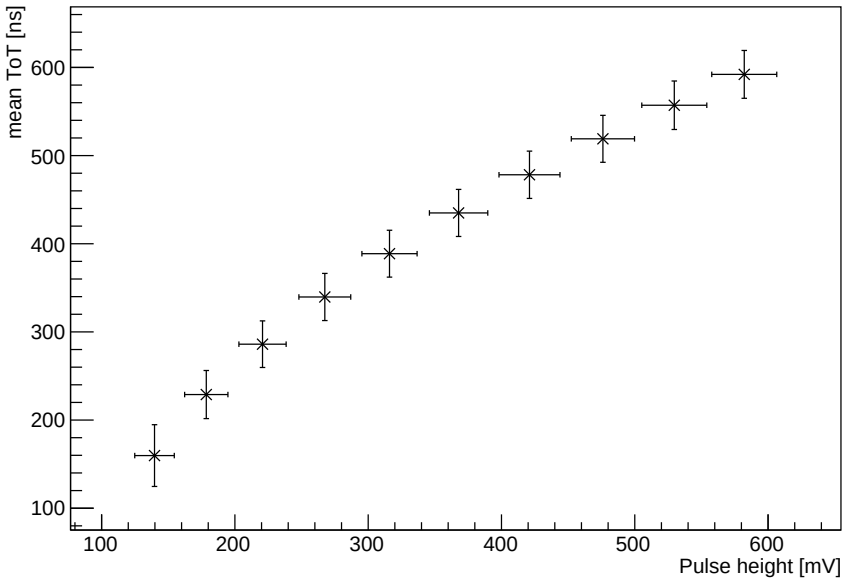

Figure 10.34: Pulseheight vs ToT for the MuPix6. Each point is for a different injection voltage (Fig. 10.32).

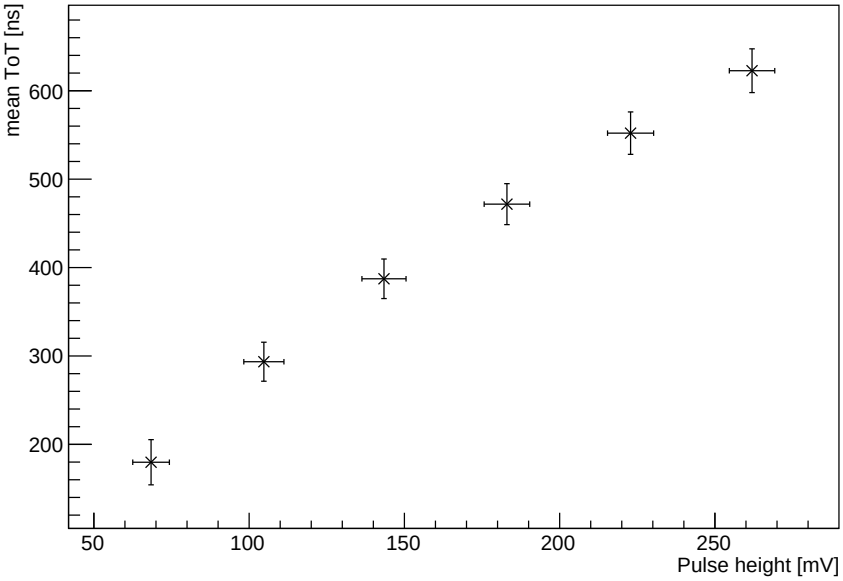

Figure 10.35: Pulseheight vs ToT for a MuPix6 pixel with one amplification stage

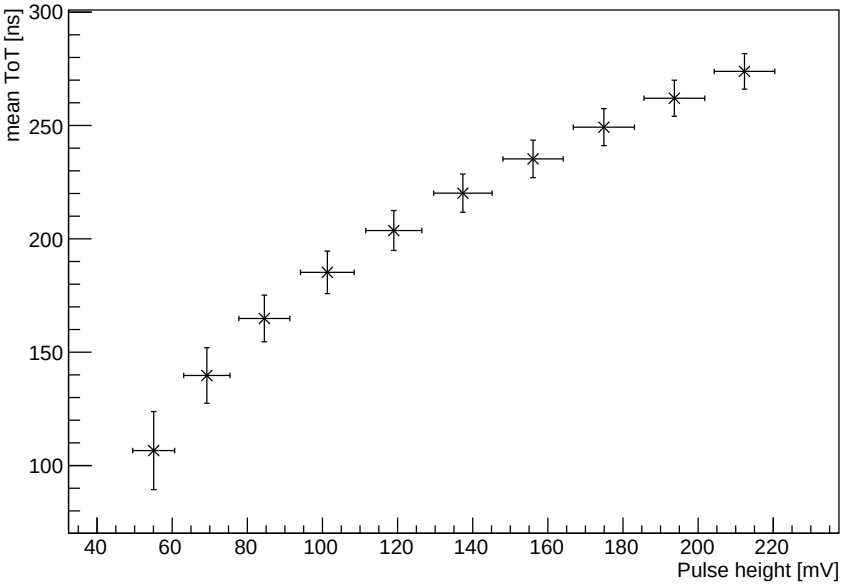

Figure 10.36: Pulseheight vs ToT for a MuPix4 pixel

Part IV

Discussion

11 Summary & Discussion

11.1 Summary

The Mu3e experiment will search for the lepton flavor violating decay $\mu^+ \rightarrow e^+e^-e^+$, which is suppressed to a branching ration of 10^{-54} in the Standard Model, so any observation of this decay would be a strong indication for physics beyond the Standard Model. The goal sensitivity of the experiment is 1 in 10^{15} muon decays which is a factor 1000 more sensitive than previously achieved for this decay [9]. To handle the high rates of low momentum decay particles, the tracker is based on High Voltage Monolithic Active Pixel Sensors (HV-MAPS). HV-MAPS combine a depleted diode as sensitive detection volume with a digital readout on the same substrate and can be thinned to 50µm without loss in sensitivity.
In this thesis two HV-MAPS prototypes for the Mu3e experiment, the MuPix4 and MuPix6, have been analyzed to quantify design changes. The newest prototype, the MuPix7 has been tested to exclude changes in the analog part compared to the MuPix6. The Time over Threshold (ToT) response to a Fe55 source of a MuPix4 and MuPix6 was measured. The structures in the ToT distribution of the MuPix4 could be attributed to the source for the main peak and field effects for the tail to short ToTs. It was further proven that results could be reliably reproduced given the same settings and conditions. The two additional peaks in the MuPix6 ToT distribution seem to be caused by a redesign of the comparator which allows short afterpulses due to an oscillation in the circuitry. The average ToT of a subset of pixels for an iron source signal was measured and no dependence on the position of the pixel on the chip was visible. However, large deviations between pixels were found which can be explained with the production uncertainties of the collection electrode.
The pulseshape of a MuPix7 and Mupix6 have been measured and were found to be in agreement with each other. Further both chips were examined in respect of their minimal detection energy with X-rays of different energies. These measurements indicate a minimal detection energy of $\approx$ 2keV which is below the expected energy deposited by the particles in the experiment with $\approx$ 4keV.
Measuring the comparator output of a pixel with only part of the amplification stages switched on revealed that the largest contribution of noise is coming from the first amplification stage or more likely the diode or sensor electrode themselves.
The relation between analog ToT and digital pulseheight was measured to show the suitability of the pulseheight as SNR measurement variable and is proportional to the energy deposition.

A tuning method was used to reduce the noise hits drastically. The threshold of each pixel was raised individually until the noise rate was below a predefined limit. The rate was reduced from over 1.5kHz per pixel to $\leq$ 1Hz per pixel for almost all pixels. The full width half maximum of the noise threshold distribution of $\approx$ 35mV was reduced to $\approx$ 10mV. This proved to be also effective while reducing the data payload significantly. Further, the results show that the method is still imperfect and can be improved as a few pixels still produce more noise than the predefined noise limit.

11.2 Discussion

The MuPix4 and MuPix6 were compared in different analog aspects and the findings were consistent with the expectations but also revealed a weakness in the MuPix6 comparator design. The oscillation found in both chips has to be addressed on future chip designs as it introduces a variance in latency and ToT.
The comparator design of the MuPix6 has to be improved as it allows short afterpulses which could be counted as hits at fast readout speeds.
Tuning for equal noise levels proved to reduce the noise rate of the pixels significant. The noise threshold distribution was also reduced in width. However the method can still be improved as some "hot" pixels remain and this method is per definition a trade off between noise and efficiency.
The approximation of the pulseshape function was verified by measuring with sources of different energies.
Measurements can be replicated given the same conditions but the setup has shown that sometimes settings are lost or not written correctly. To analyze this problem it should be possible to read the chip and test board settings back, which is foreseen for future prototypes. Currently, the chip can't copy its settings and send them out which should be implemented to monitor the conditions for data acquisition during the experiment.

11.3 Outlook

All tests with the MuPix7 had very positive results, which allows for a full readout implementation of the detector in the lab. If the MuPix7 fulfills all specifications of its digital features, the next chip could be a first large prototype which could be used for the detector. The comparator however should to be redesigned to prevent afterpulses has to be thoroughly investigated to find and remove the source of the oscillation seen on the comparator output.
In the future also other substrate resistivites and production processes could be used to achieve a larger depletion zone and with that a higher signal. This would result in a a better SNR, which in turn increases the efficiency.

Part V

Appendix

12 Appendix

12.1 Chip DAC values

The DAC values are shown in hexadecimal.
For the BlRes values in Tab. 12.2, 5 instead of A like in [16] was used [43].
The comparison between the MuPix4 (Tab. 12.1) and the MuPix 6 high power settings (Tab. 12.2) show only a few changes. The BlRes values have been reduced and THRes has been set to 0. THRes is not included in the MuPix6 analog layout anymore but its register was left to ensure backwards compatibility [43].
VPDAC is always set to 0 by default because it's not necessary for operating the chip and depends on the chip and the tuning method.

DAC Settings	
DAC	Value [hex]
VPDAC	0
VPComp	3C
VNDel	A
VNLoad	5
VNFoll	A
VNFB	A
VN	3C
THRes	3C
BLRes	3C

Table 12.1: MuPix4 DAC settings from [23]

DAC Settings		
DAC	High Power [hex]	Low Power [hex]
VPDAC	0	0
VPComp	3C	A
VNDel	A	A
VNLoad	5	2
VNFoll	10	A
VNFB	A	3
VN	3C	5
THRes	0	0
BlRes	5	5
VNLoad2	5	2
VNFB2	A	3
VN2	3C	5
BlRes2	5	5

Table 12.2: MuPix6 DAC settings from [16]

12.2 Silicon Properties

Property		Value	Unit
Atomic number	Z	14	
Nucleon number	28.09		
Density	ρ	2.33	g/cm^3
Crystal structure		Diamond	
Atom density		5.02	cm^{-3}
Intrinsic charge density	1.5×10^{10}	$1/cm^3$	
Dielectric constant	ϵ	11.9	
	at 300K		
Band gap	indirect band gap	1.12	eV
	direct band gap	3.4	eV
Average creation energy for an electron-hole pair	ω	3.66	eV
Fano Factor	F	0.115	
Mobility	μ_n	1450	cm^2s/V
	μ_p	500	cm^2s/V

Table 12.3: Important silicon properties [27, 39, 44, 45, 46, 47].

Bibliography

[1] A. Blondel *et al.* *Research Proposal for an Experiment to Search for the Decay $\mu \to eee$. ArXiv e-prints*, **2013**. 1301.6113. ↑13, 21

[2] Wikimedia Commons. *Standard Model of Elementary Particles*, **2014**. Accessed 10 July-2015, URL: http://en.wikipedia.org/wiki/File:Standard_Model_of_Elementary_Particles.svg. ↑15, 101

[3] G. Aad *et al.* (ATLAS Collaboration). *Observation of a new particle in the search for the Standard Model Higgs boson with the ATLAS detector at the LHC.* **2012**. 1207.7214. ↑16

[4] S. Chatrchyan *et al.* (CMS Collaboration). *Observation of a new boson at a mass of 125 GeV with the CMS experiment at the LHC. Phys.Lett.B*, **2012**. 1207.7235. ↑16

[5] Q. R. Ahmad *et al.* (SNO Collaboration). *Measurement of the charged current interactions produced by B-8 solar neutrinos at the Sudbury Neutrino Observatory. Phys. Rev. Lett.*, **87**: p. 071301, **2001**. nucl-ex/0106015. ↑16

[6] F.P. An *et al.* (Daya Bay Collaboration). *Observation of electron-antineutrino disappearance at Daya Bay. Phys.Rev.Lett.*, **108**: p. 171803, **2012**. doi:10.1103/PhysRevLett.108.171803. 1203.1669. ↑16

[7] Y. Fukuda *et al.* (Super-Kamiokande Collaboration). *Evidence for oscillation of atmospheric neutrinos. Phys. Rev. Lett.*, **81**: pp. 1562–1567, **1998**. hep-ex/9807003. ↑16

[8] K.A. Olive et al. (Particle Data Group). *The Review of Particle Physics. Chin. Phys. C, 38, 090001 (2014).*, **2014**. ↑17, 26, 28, 101

[9] U. Bellgardt *et al.* (SINDRUM Collaboration). *Search for the Decay $\mu^+ \to e^+e^+e^-$. Nucl.Phys.*, **B299**: p. 1, **1988**. doi:10.1016/0550-3213(88)90462-2. ↑17, 20, 91

[10] J. Adam *et al.* (MEG Collaboration). *New Constraint on the Existence of the $\mu^+ \to e^+\gamma$ Decay. Phys. Rev. Lett.*, **110**: p. 201801, **May 2013**. doi:10.1103/PhysRevLett.110.201801. ↑17

[11] W. J. Marciano, T. Mori and J. M. Roney. *Charged Lepton Flavor Violation Experiments. Ann.Rev.Nucl.Part.Sci.*, **58**: pp. 315–341, **2008**. doi:10.1146/annurev.nucl.58.110707.171126. ↑19, 101

[12] L.M. Brarkov *et al. Search for $\mu^+ \to e^+\gamma$ down to 10^{-14} branching ratio. Research Proposal to PSI*, **1999**. ↑20

[13] J. Kaulard *et al.* (SINDRUM II Collaboration). *Improved limit on the branching ratio of $\mu^- \to e^+$ conversion on titanium. Phys.Lett.*, **B422**: pp. 334–338, **1998**. doi:10.1016/S0370-2693(97)01423-8. ↑20

[14] J. Ashkin H. A. Bethe. *Passage of radiation through matter. Nucl. P*, **1**: p. 253, **1953**. ↑25

[15] S. M. Seltzer and M. J. Berger. *Improved Procedure for Calculating the Collision Stopping Power of Elements and Compounds for Electrons and Positrons. The International Journal of Applied Radiation and Isotopes*, **35**, **1984**. ↑27, 101

[16] H.Augustin. *Characterization of a novel HV-MAPS Sensor with two Amplification Stages and first examination of thinned MuPix Sensors.* Master Thesis, Heidelberg University, **2014**. ↑27, 33, 39, 41, 43, 44, 47, 51, 54, 57, 60, 61, 64, 67, 68, 73, 78, 85, 95, 96, 101, 102, 105

[17] William R. Leo. *Techniques for nuclear and particle physics experiments.* Springer, **1987**. ISBN: 3-540-17386-2 ; 0-387-17386-2 ; 978-0-387-17386-3 ; 978-3-540-17386-1. ↑28

[18] Wikimedia Commons. *PN-junction equilibrium*, **2014**. Accessed 10 July 2015, URL: https://upload.wikimedia.org/wikipedia/commons/d/d6/Pn-junction-equilibrium.png. ↑32, 101

[19] J. Baudot et al. *First test results Of MIMOSA-26, a fast CMOS sensor with integrated zero suppression and digitized output.* (pp. 1169 –1173), **24 2009-nov. 1 2009**. ISSN: 1095-7863. doi:10.1109/NSSMIC.2009.5402399. ↑35

[20] I. Rubinskiy. *An EUDET/AIDA Pixel Beam Telescope for Detector Development. Physics Procedia*, **37**, 0: pp. 923 – 931, **2012**. ISSN: 1875-3892. doi:http://dx.doi.org/10.1016/j.phpro.2012.02.434. Proceedings of the 2nd International Conference on Technology and Instrumentation in Particle Physics (TIPP 2011), URL: http://www.sciencedirect.com/science/article/pii/S1875389212017889. ↑35

[21] Ivan Perić. *A novel monolithic pixelated particle detector implemented in high-voltage CMOS technology. Nuclear Instruments and Methods in Physics Research Section A: Accelerators, Spectrometers, Detectors and Associated Equipment*, **582**, 3: pp. 876 – 885, **2007**. ISSN: 0168-9002. doi:10.1016/j.nima.2007.07.115. ↑36, 101

[22] R. Philipp. *Characterisation of High Voltage Monolithic Active Pixel Sensors for the Mu3e Experiment.* Master Thesis, Heidelberg University, **2014**. ↑39, 47, 54, 61, 64, 85

[23] F. Förster. *HV-MAPS Readout and Direct Memory Access for the Mu3e Experiment.* Master Thesis, Heidelberg University, **2014**. ↑40, 61, 95, 105

[24] L. Huth. *Development of a Tracking Telescope for Low Momentum Particles and High Rates consisting of HV-MAPS*. Master Thesis, Heidelberg University, **2014**. ↑40, 47, 51

[25] A.-K. Perrevoort. *Characterisation of High Voltage Monolithic Active Pixel Sensors for the Mu3e Experiment*. Master Thesis, Heidelberg University, **2012**. ↑44, 46, 102

[26] H. Augustin. *Charakterisierung von HV-MAPS*. Bachelor Thesis, Heidelberg University, **2012**. ↑44

[27] Helmuth Spieler. *Semiconductor detector systems*. Series on semiconductor science and technology ; 12 ; Oxford science publications ; Series on semiconductor science and technology. Oxford Univ. Press, Oxford [u.a.], **2008**, repr. edition. ISBN: 978-0-19-852784-8. ↑44, 45, 96, 105

[28] Dirk Wiedner. *MuPix Test PCB Develoment*. Personal Contact. ↑47

[29] Keithley Instruments Inc. *High Voltage power supply series 2600 B*. URL: https://www.keithley.de/products/dcac/currentvoltage/2600B/?path=2604B/Documents#4. ↑49

[30] HAMEG Instruments. *Power supply HMP 4030 HMP 4040*. ↑49

[31] Niklaus Berger. *MuPix Firmware*. Internal. ↑50

[32] M. Kiehn. *FPGA driver*. Private Communication. ↑50

[33] Frank Gray. *Pulse code communication*, **1953**. ↑50

[34] Qt Project. *Qt Project*, **2014**. URL: http://qt-project.org/. ↑51

[35] Boost. *Boost c++ libraries*, **2014**. URL: http://www.boost.org/. ↑51

[36] PHYWE. *Operating Instructions for the PHYWE XR 4.0 expert unit, X-ray unit, 35kV*. URL: pository.phywe.de/files/bedanl.pdf/09057.99/e/0905799e.pdf. ↑53, 102

[37] *Praktikumsanleitung zum Physikalischen Praktikum für Studierende der Medizin und Zahnmedizin an der Ruprecht-Karls-Universität Heidelberg*, **March 2014**. ↑53, 59

[38] AMS. *AMS 0.18µm HV-CMOS Process Parameters*. ↑58, 74, 85

[39] J.C. Ashley. *Energy loss rate and inelastic mean free path of low-energy electrons and positrons in condensed matter*. *Journal of Electron Spectroscopy and Related Phenomena*, **50**, 2: pp. 323 – 334, **1990**. ISSN: 0368-2048. doi:http://dx.doi.org/10.1016/0368-2048(90)87075-Y. URL: http://www.sciencedirect.com/science/article/pii/036820489087075Y. ↑58, 96, 105

[40] NIST. *XCOM photon cross section library*, **2014**. Extracted 08.07.15, URL: http://physics.nist.gov/PhysRefData/Xcom/html/xcom1.html. ↑62, 102

[41] PHYWE. *Charactristische Röntgenstrahlung von Wolfram*. URL: http://www.phywe-es.com/index.php/fuseaction/download/lrn_file/versuchsanleitungen/P2542801/d/p2542801d.pdf. ↑75, 76, 103

[42] J. Philipp. *Effizienzanalyse von HV-MAPS anhand des MuPix-Teleskops*. Bachelor Thesis, Physics Institute Heidelberg, **2015**. In Progress. ↑85

[43] H.Augustin. *DAC Values*. Private Communication. ↑95

[44] Martin A. Green. *Intrinsic concentration, effective densities of states, and effective mass in silicon*. *Journal of Applied Physics*, **67**, 6: pp. 2944–2954, **1990**. doi: http://dx.doi.org/10.1063/1.345414. URL: http://scitation.aip.org/content/aip/journal/jap/67/6/10.1063/1.345414. ↑96, 105

[45] B.G. Lowe and R.A. Sareen. *A measurement of the electron-hole pair creation energy and the Fano factor in silicon for 5.9keV X-rays and their temperature dependence in the range 80-270K*. *Nuclear Instruments and Methods in Physics Research Section A: Accelerators, Spectrometers, Detectors and Associated Equipment*, **576**: pp. 367 – 370, **2007**. ISSN: 0168-9002. doi:http://dx.doi.org/10.1016/j.nima.2007.03.020. URL: http://www.sciencedirect.com/science/article/pii/S016890020700527X. ↑96, 105

[46] H. Philipp and E. Taft. *Optical Constants of Silicon in the Region 1 to 10 ev*. *Phys. Rev.*, **120**: pp. 37–38, **Oct 1960**. doi:10.1103/PhysRev.120.37. URL: http://link.aps.org/doi/10.1103/PhysRev.120.37. ↑96, 105

[47] F. Scholze, H. Henneken *et al.* *Determination of the electron-hole pair creation energy for semiconductors from the spectral responsivity of photodiodes*. *Nuclear Instruments and Methods in Physics Research Section A: Accelerators, Spectrometers, Detectors and Associated Equipment*, **439**, 2-3: pp. 208 – 215, **2000**. ISSN: 0168-9002. doi:http://dx.doi.org/10.1016/S0168-9002(99)00937-7. URL: http://www.sciencedirect.com/science/article/pii/S0168900299009377. ↑96, 105

List of Figures

List of Tables

Acknowledgments

At the end of this thesis I would like to thank everyone who supported me and helped me to get this far.

I want to thank Prof. Dr. André Schöning first for giving me the opportunity to work for the Mu3e experiment. Also, I want to thank Priv. Doz. Dr. Ulrich Schmidt for agreeing to be my second examiner.

Additionally I want to thank:

- Jonathan Philipp for enduring me during the years of our Bachelor studies
- Dirk Wiedner for his support and almost always knowing the answer before I finished asking
- Heiko Augustin for teaching almost everything I know about the MuPix
- Lennart Huth for questioning my methods in a constructive way

I want to thank the rest of Mu3e Heidelberg for their support and companionship.

At last, I thank my parents, family and friends. Without them I wouldn't have made it to this point.

Erklärung:

Ich versichere, dass ich diese Arbeit selbstständig verfasst habe und keine anderen als die angegebenen Quellen und Hilfsmittel benutzt habe.

Heidelberg, den 14.07.2015 .....